Master thesis : Aerodynamic Stability of Pelycosaurs

Auteur : Laurent, Thibault
Promoteur(s) : Dimitriadis, Grigorios
Faculté : Faculté des Sciences appliquées
Diplôme : Master en ingénieur civil en aérospatiale, à finalité spécialisée en "aerospace engineering"
Année académique : 2018-2019
URI/URL : http://hdl.handle.net/2268.2/8281

Université de Liège
Master in aerospace engineering
Academic year 2018-2019

Aerodynamic stability of pelycosaurs

Master thesis

Author:
Thibault LAURENT

Supervisor:
G. DIMITRIADIS

President of the Jury:
J-P. PONTHOT

Members of the Jury:
T. ANDRIANNE
G. DIMITRIADIS
R. NUDDS

Liège
August 2019

Abstract

This thesis aims to study the aerodynamic stability of pelycosaurs, a group of Paleozoic reptiles that featured a large neural spine sail for thermoregulatory purposes. If the presence of such a fin would allow the animal's body temperature to be regulated, it would however certainly lead to a generation of significant aerodynamic loads and then influence their stability in case of high wind speeds. Therefore, numerical and experimental analyses of the airflow around a selected specimen are performed to determine if a high sustained wind could make it topple.

After the selection of a representative geometry derived from an existing skeleton, a numerical model of the sail is built using the vortex lattice method, based on the potential flow theory. The problem discretization is addressed and a convergence study of the model is performed to select the most optimal parameters. The limits of such a method are determined by comparing its results with the ones obtained by a physical model based on the same geometry and tested in a state-of-the-art wind tunnel. The comparison shows that the two models give very similar results when the sail is exposed to the airflow at low angles of attack (< 10 degrees), then the numerical values begin to diverge but remain close from the experimental ones as the angle increase to eventually completely disagree with reality starting from 45 degrees.

A finite element model of the sail is then realized, once again based on the representative geometry. The bones are modelled as 3D beams and decomposed in an optimal number of finite elements to estimate their deformation and internal stresses when subject to loads. This model is then coupled with the VLM one for two reasons: the determination of the deformed shape when the sail is subject to the aerodynamic loads obtained by the VLM at various wind speeds and angles of attack, and the influence of this new shape on the aerodynamic loads. This section shows that the sail is very rigid since it hardly deforms even at very high wind speeds and high angles of attack.

Finally, the stability analysis is made on a complete model of the animal, considering a full-grown specimen. Two body configuration are studied: the regular position of the reptile and its possible position when reacting to a big destabilizing moment. It results that the considered pelycosaur is very stable, since it is impossible to topple at low angles of attack and only the most critical weather condition on the Beaufort scale could endanger its stability at high angles of attack, for both positions. In conclusion, the existence of its large sail without compromising the stability is then made possible because of its heavy weight and low centre of gravity.

Acknowledgment

I would like to express my deepest appreciation to my supervisor Professor Grigorios Dimitriadis for giving me the opportunity to work on this original and instructive project. I am forever grateful for his guidance and wise advice, but also for his numerous ideas that helped to shape this thesis. I would also like to address a special thank you to Dr. Thomas Andrianne for his availability and help during the wind tunnel tests.

My thanks also go to all the professors, assistants and staff that I encountered during all these years for the knowledge and enthusiasm for sciences they shared with us. To all my friends who made this stage of my life so rich, thank you.

I would finally like to thank my family for their priceless support and encouragements during my studies.

Contents

List of Figures

Chapter 1

Introduction

1 Context and motivation

Since the beginning of time, the animal evolution allows species to adapt themselves and survive to their changing environment and sometimes leads to the development of very ingenious but also curious body parts. This is the case of the pelycosaurs, a group of Paleozoic synapsids, also called "mammal-like reptiles" since, despite their reptile appearance, they are more closely related to mammals than to today reptiles. Their particularity is that some members of this family featured a large neural spine sail on their back, composed by long spines extending from the vertebrae. The most probable function of this device is the thermoregulation of the animal's body, using its large surface to capture the solar rays and using convection to exchange heat with the external world. Depending on the genus, the size of the sail with respect to the body could become important, and often the sail's surface was proportional to the body size.

The existence of such a large sail inevitably has consequences on the aerodynamic profile of the pelycosaur, generating aerodynamic loads that could endanger its stability in case of high winds. The aim of this study is then to consider the sail's contribution to the global equilibrium of the animal and determine whether if the animal could live in every weather condition or if having this thermoregulatory body part limited it to move only in case of calm weather. The study will be focused on a subfamily of the pelycosaurs, the dimetrodon, which was the largest ranging in length from 1.7 to 4.6 metres, and weighing between 28 and 250 kilograms [1].

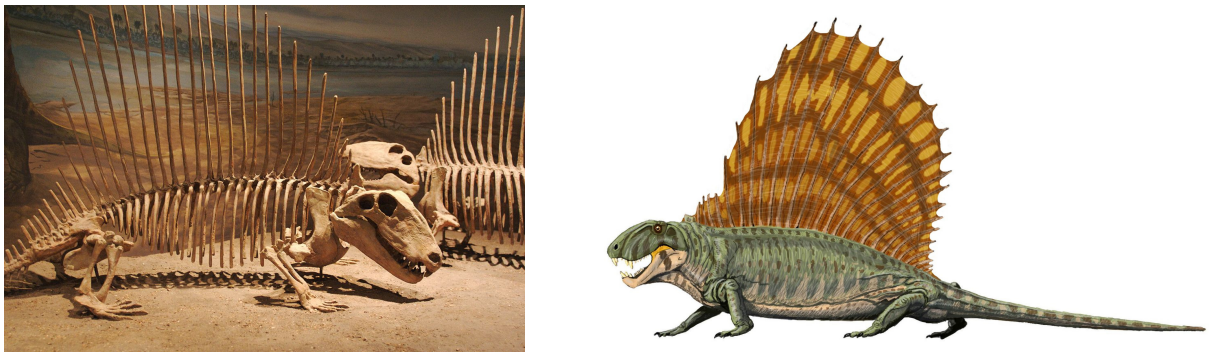

Figure 1.1: Skeleton and illustration of the dimetrodon (source: Wikipedia).

To do so, a numerical analysis of the flow around a selected geometry will first be performed using the Vortex Lattice Method (VLM). The latter uses the potential flow theory, and thus

has several assumptions that limit the result accuracy. This is why the second step will consist in the comparison of the values obtained with this numerical model with a physical one, based on the same geometry. The latter will be a scaled version of the sail that will be tested in a state-of-the-art wind tunnel to find the belonging aerodynamic characteristics. The numerical and experimental results will then be compared and the limits of the VLM will be determined.

The next step will be the finite element analysis of the sail to account for the possible deformation of the sail under substantial loading. The bones will be modelized as 3D beams, and the model will allow the computation of the estimated displacements and internal stresses. A flexible model will then be implemented by coupling the finite element model with the VLM one so that the deformation of the sail under aerodynamic loading can be computed and the new aerodynamic properties of this deformed shape can be investigated.

Finally, a stability analysis of the selected dimetrodon will be performed, considering wind speeds from low to high (calm to stormy weather), and considering different positions of the animal with respect to the airflow direction.

2 Selection of the representative sail geometry

In order to make consistent comparisons between numerical simulations and wind tunnel tests, a specific geometry has to be chosen. As mentioned previously, several species were identified in the pelycosaurs family. Among them, the dimetrodon was the largest and also had the biggest sail. In consequence, it should then generate the most important aerodynamic loads and was more likely to experience difficulties in case of bad weather. Since the size and shape of the sail vary with the species and individual, an arbitrary dimetrodon skeleton is selected for the following parts of this thesis from the literature (Figure 1.2).

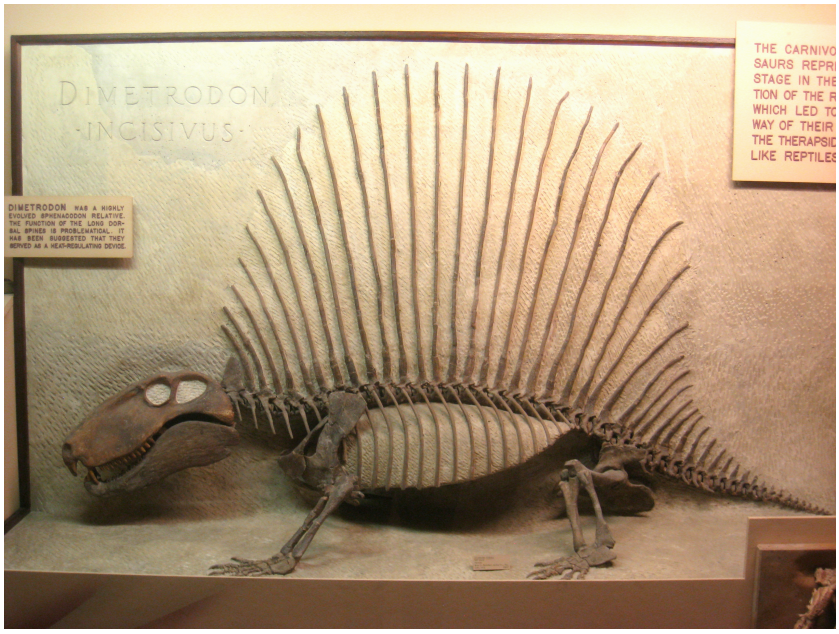

Figure 1.2: Skeleton of the dimetrodon at the University of Michigan Museum of Natural History.

The geometry of the sail will be retrieved and used for the aerodynamic loads' prediction, the fin's bones size and diameter will be used to estimate the deformations due to those loads and the length of the legs' bones will be used to compute the overturning moment.

Chapter 2

Vortex Lattice Method

Now that the geometry is selected, a first analysis will be made using the vortex lattice method (VLM). It is a numerical approach, based on potential flows, which is commonly used in the preliminary step of aerodynamic projects, most of the time involving wing design. It performs well to predict the aerodynamic loads in incompressible and attached flows.

The advantages of this method are its simple implementation and its low computational cost. However, the drawback is the lack of accuracy of the results compared for example to a complete CFD analysis, due to its strong assumptions. If the basics of the VLM will be explained in this chapter, a more complete description is given by Katz and Plotkin in [2].

1 Reminder of potential flows

The vortex lattice method being based on the theory of potential flow, it means that it considers four important assumptions in order to use the Laplace equation.

- The flow is considered inviscid, meaning that the viscous effects are not handled,
- the flow is steady,
- the flow is incompressible,
- the flow is irrotational.

All those hypotheses have several consequences that differentiate the model from reality. Besides neglecting the friction drag, the inviscid and irrotational flow has to remain attached from the leading edge to the trailing edge. It means that the situation of flow separation, appearing as the angle of attack of the sail increases, will be badly represented by the potential flow theory. This problem will be studied later when comparing the VLM to the wind tunnel results. On top of that, the condition of flow steadiness means that the sail should not move during the simulations. This is not a problem since a steady case is considered in this thesis. Moreover, it also means that the flow has to be steady, implying that only sustained winds are considered.

Now that the hypotheses are established, the potential flow problem can be solved using Laplace's equation. The velocity potential Φ is defined as

$$\nabla\Phi = \vec{V}, \tag{2.1}$$

where $\vec{V}$ is the velocity field. The Laplace's equation then becomes

$$\Delta\Phi = 0. \tag{2.2}$$

The problem can be solved using elementary solutions, which are algebraic functions of unknown strength satisfying Laplace's equation. The objective is to superimpose them to re-create the flow around a physical object. The four principal types of elementary solutions are the uniform flow, the source/sink flow, the doublet flow and the vortex flow. With this methodology, the problem is made easier to solve since it is now a limit value calculation expressed as a set of algebraic equations for an unknown distribution of singularities over a certain surface.

The Laplace's equation being of second-order, it requires two boundary conditions. The first is the impermeability on the body surface, meaning that the flow velocity normal to the surface has to be equal to zero, so that

$$V \cdot n = 0. \tag{2.3}$$

The second one is the undisturbed far-field, meaning that the influence of the flow should vanish at an infinite distance, so that

$$\vec{\nabla}\Phi|_\infty = \vec{V}_\infty. \tag{2.4}$$

Finally, the Kutta condition can be added, since a lifting body is considered, to impose a smooth exit of the flow at the trailing edge, and then enforce a real effect (viscosity) in the potential flow theory.

In short, the aim of the potential flow is then to replace the complex differentiation problem with an algebraic one, by using elementary solutions that satisfy Laplace's equation. The boundary conditions are then applied so that eventually a unique solution is determined.

2 Description of the Vortex Lattice Method

The principle of the Vortex Lattice Method is to divide the lifting surface into panels on which lies vortex rings, also called vortex lattices. A vortex ring is a rectangle composed of four vortex segments, with no thickness. The latter is an elementary solution of Laplace's equation that was described just before. The advantage of this element is that it requires a simple programming effort.

The vorticity Γ is constant along the 4 segments of the ring and is defined with respect to the right-hand rotation rule. The normal vector $\mathbf{n}$ is defined at the centre of the vortex ring, also called the collocation point. A vortex ring is associated with each panel (also called bound vortices), with the leading segment placed exactly at the quarter chord of the panel, as shown in Fig.2.1. The collocation point is then at the centre of the three-quarter chord line. Each segment is inducing a velocity $\mathbf{q}$ at an arbitrary point P(x,y,z) (Fig.2.2). If the point is located on a vortex segment, the induced velocity is equal to 0.

The velocity induced on a panel's collocation point by a vortex ring is computed using the Biot-Savart law, stating that

$$\mathbf{q} = \frac{\mathbf{\Gamma}}{4\pi} \oint_C \frac{d\mathbf{l} \times \mathbf{r}}{r^3}, \tag{2.5}$$

where C is the vortex ring contour, $\mathbf{r}$ the vector from the collocation point to the vortex segment considered and $\mathbf{\Gamma}$ the ring's vortex strength. The matrices of influence A_{cl} and A_{cw}, corresponding respectively to the influence of the lifting surface and wake panels, are calculated using the projection of the velocity induced $\mathbf{q}_{ij}$ by each panel onto the normal direction $\mathbf{n}_i$ of the collocation point i;

$$(A_{cl})_{ij} = \mathbf{q}_{ij} \cdot \mathbf{n}_i \qquad i = 1...M, j = 1...N \tag{2.6}$$

$$(A_{cw})_{ij} = \mathbf{q}_{ij} \cdot \mathbf{n}_i \qquad i = 1...W, j = 1...N \tag{2.7}$$

where M is the number of panels in the chordwise direction, N in the spanwise direction and W is the number of panels present in the wake.

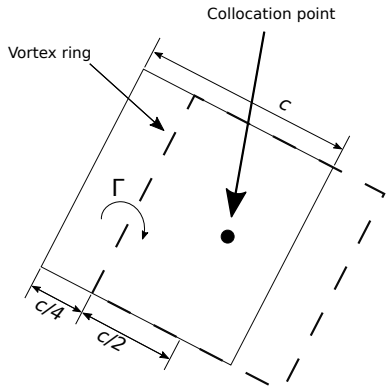

Figure 2.1: View of a single surface panel and its associated vortex ring.

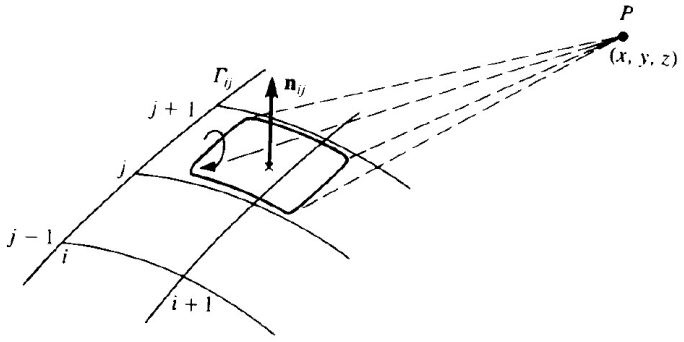

Figure 2.2: Vortex ring element and its influence at point P. Illustration from [2]

The vortex lattice method is here solved with a time-marching algorithm, and at the beginning, only the lifting surface bound vortex rings exist (the wake panels are not shed yet). The last segment of the trailing edge will represent the starting vortex. At each time step, the vorticities Γ of each wing panel are calculated by enforcing the impermeability condition cited before, saying that the panel has no flow in the normal direction at its collocation point. This is traduced mathematically by

$$A_{cl}\mathbf{\Gamma}_l + A_{cw}\mathbf{\Gamma}_w + \mathbf{w} = 0, \tag{2.8}$$

where $\mathbf{w}$ is the velocity of the free stream in the collocation point's normal direction.

The Kutta condition, indicating that the flow must separate at the trailing edge is automatically satisfied by placing the leading edge of each vortex ring at the quarter chord of its associated panel.

The first time step is executed without any wake panel. During the second time step, as the flow is moving along the lifting surface, each trailing edge vortex panel sheds a wake panel, having a vortex strength (Γ_w^{n+1}) equal to the T.E. circulation at the previous time step ($\Gamma_{T.E.}^{n}$). This methodology, shown in Fig.2.3 and Fig.2.4, can then be repeated to study the influence of a longer wake. Since the vorticity of the wake panels does not change in time, the only unknowns remaining are the wing bound vortices, and can then be calculated for the following time step by applying the boundary conditions on the same collocation points.

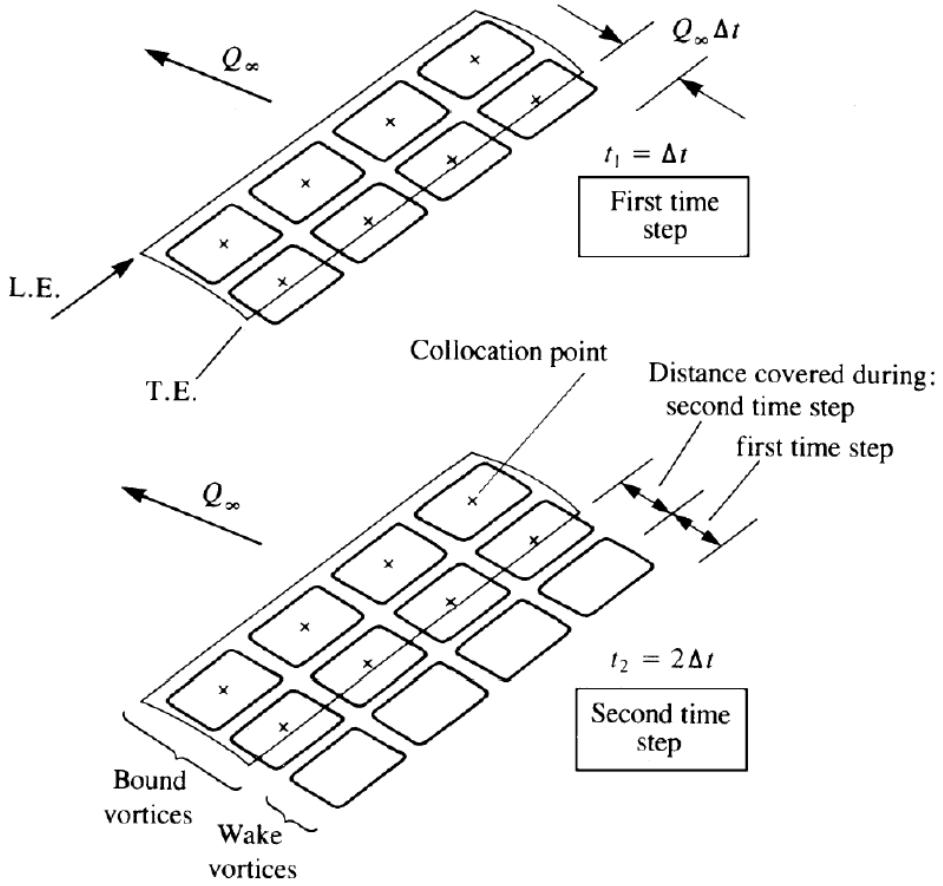

Figure 2.3: Vortex ring model for the lifting surface during the first time step (upper figure) and during the second time step (lower figure). Illustration from [2]

The shedding of the wake can either follow a free wake or a flat wake model. In a free wake model, the vortex rings are shed freely and deforms with respect to the local flow (the ring's corner points are moved by the local velocity, as depicted by Fig.2.4), simulating the wake roll-up. This method gives a wake shape close to reality but is time consuming compared to the flat wake model. In this second approach, the free stream simply convects the wake without any deformation.

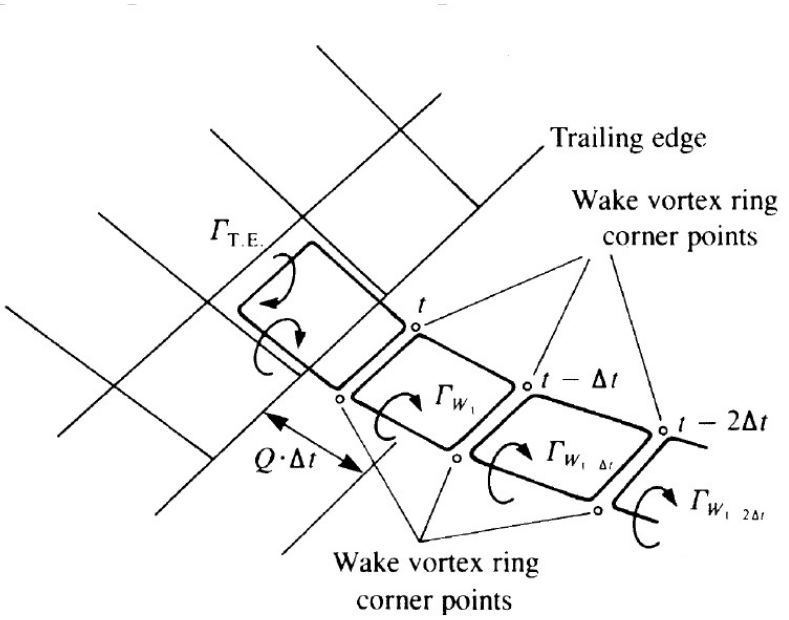

Figure 2.4: Nomenclature for the wake shedding procedure at a typical trailing-edge panel. Illustration from[2].

Finally, the aerodynamic loads of each bound vortex segment are found using the Joukowski theorem:

$$\delta \mathbf{F} = \rho \Gamma_{\delta \mathbf{l}} (\mathbf{U} \times \delta \mathbf{l}) \tag{2.9}$$

where $\delta \mathbf{l}$ is the vortex segment, $\Gamma_{\delta \mathbf{l}}$ its circulation and U the vector of local velocity corresponding to the segment $\delta \mathbf{l}$.

3 Matlab implementation

The computations for the vortex lattice method are executed on *Matlab*. The code is largely based on the one developed by G. Dimitriadis in [3] for the calculations of induced drag for cambered wings.

The first step is to specify the studied geometry and the parameters, which are:

- the number of wings (1 or 2),
- the number of panels in the spanwise and chordwise direction,
- the airspeed and its direction,
- the angle of attack,
- the air density,
- the length of the studied domain (and thus of the wake length taken into account in the computations).

Then, the wing discretization is performed with the entered parameters by defining the geometric panels. The vortex rings corner points are calculated, placing their leading edge at the panels' quarter-chord. The position of the collocation points used for the calculation is then determined, as well as their normal and tangent vectors.

The next step consists in the shedding of the vortex elements. Follows the determination of the influence matrices and the external velocities. The wake vorticity computed at the previous time step allows to calculate the velocity induced by the wake at the collocation points determined before. The bound vorticity is then found using the impermeability condition. Later, the contribution of the induced velocities coming from the wing's bound vorticity is added. The 3 components of the forces are finally calculated using the Joukowski method (Eq.(2.9)).

The final step is the propagation of the wake. If the wake roll-up is chosen, the vortex ring corner points are propagated with the local velocity. Otherwise, in the case of a flat wake, the wake is propagated with the free stream. The routine is then repeated for each time step. The number of time steps is specified by the user, depending on the studied domain's lengths and the discretization.

4 Problem discretization

The "wing" geometry is based on the representative sail selected in chapter 2. The contour of the skeleton is defined and then implemented on *Matlab*, the dimetrodon's fin being seen as a thin symmetric half-wing.

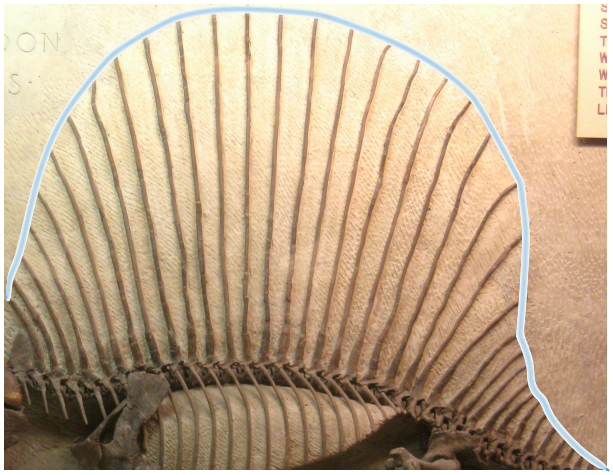

Figure 2.5: View of the representative sail and its contour in *Matlab*.

The division of the geometry into panels is now addressed. This stage is crucial because a bad discretization leads to irrelevant results. It concerns the length of the domain and the studied wake as well as the number of division in the spanwise and chordwise direction. The number of panels in the spanwise direction per half-wing will be denoted N and the number of panels in the chordwise direction will be denoted M.

The geometry on which the forces and then the aerodynamic coefficients are computed is, in fact, a "2 wings configuration", the sail and its panels are mirrored by symmetry with respect to the chord. The objective is to model the ground, and only have wingtip vortices at the extremity of the sail. The final values of the lift and drag coefficients are then simply divided by two. The values presented throughout this thesis are the ones corresponding to the sail, so after the division.

The panels distribution in the spanwise direction follows a growth rate, to better capture the effects at the wingtip. A typical model with 20 panels spanwise and 15 chordwise is shown in Fig.2.6. The bounded vortex rings and their collocation point are represented in red.

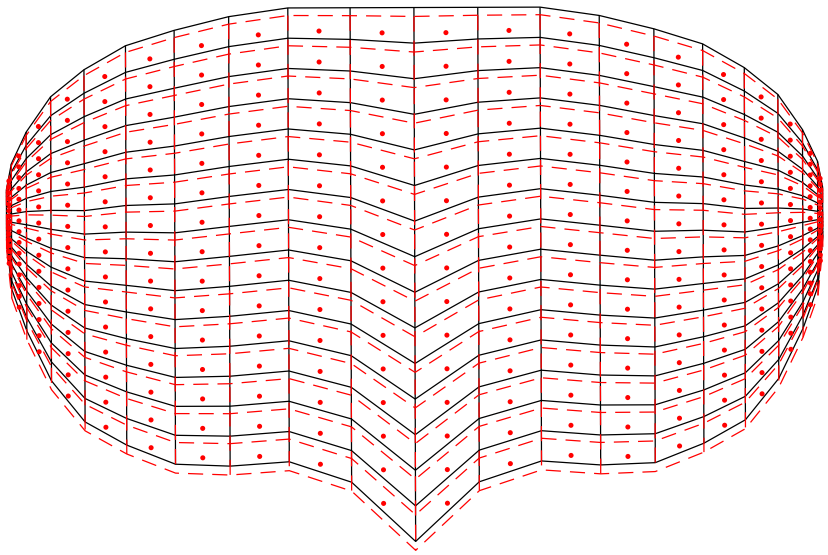

Figure 2.6: Display of the VLM model with N=10, M=15 and its bounded vortex rings.

4.1 Time step

The time step used in the simulations is defined as follow:

$$\Delta t = \frac{c}{MU_\infty}, \tag{2.10}$$

where c is the length of the chord root, M the number of chordwise panels and U_∞ the airspeed. This definition aims to ensure that the wake panels get the same area than the trailing edge panels they are shed from. This gives a smooth transition from the wing to the wake and allows to refine the wake by increasing the number of chordwise divisions.

4.2 Domain

The wake contains a certain amount of circulation, which have a significant effect on the aerodynamic forces. It is then important to make sure that most of its influence is captured, by selecting a domain that is large enough. Simulations are done on 2, 5, 10 and 15 chord lengths domains, and the resulting total 3D aerodynamic coefficients at an angle of attack of 10 degrees are compared in the Tab. 1. It should be reminded that the values displayed are the ones from the two wings configuration divided by two, in order to remove the contribution of the mirrored wing. A fast convergence of the results can be observed, as the CPU time increases quickly as well. A domain of 5 chord lengths is chosen, giving reliable values for an acceptable CPU time.

Number of chords	C_L	C_D	CPU time - [s]
2	0.4886	0.0278	25
5	0.4934	0.0271	138
10	0.4935	0.0271	722
15	0.4935	0.0271	2130
20	0.4935	0.0271	4786

Table 1: Variation of the aerodynamic coefficients and CPU time of the VLM model for various domain lengths.

4.3 Number of spanwise panels

The domain being selected, the number of panels in the chordwise and spanwise directions has to be defined. A study of convergence is performed, using once again the aerodynamic coefficients as indicators. It is essential to wisely choose the number of division since a too coarse mesh can give inaccurate results while a too fine one would take forever to compile. In addition to refining the grid quality, increasing the number of panels in the spanwise direction improves the wingtip effects modelling while increasing the number of panels in the chordwise direction improves the wake modelling (due to the time step definition in Eq.(2.10)).

First, the test of convergence is done by varying the number of spanwise panels. As shown by Fig.2.7, the value of the lift and drag coefficients globally converge, until 20 divisions per half-wing.

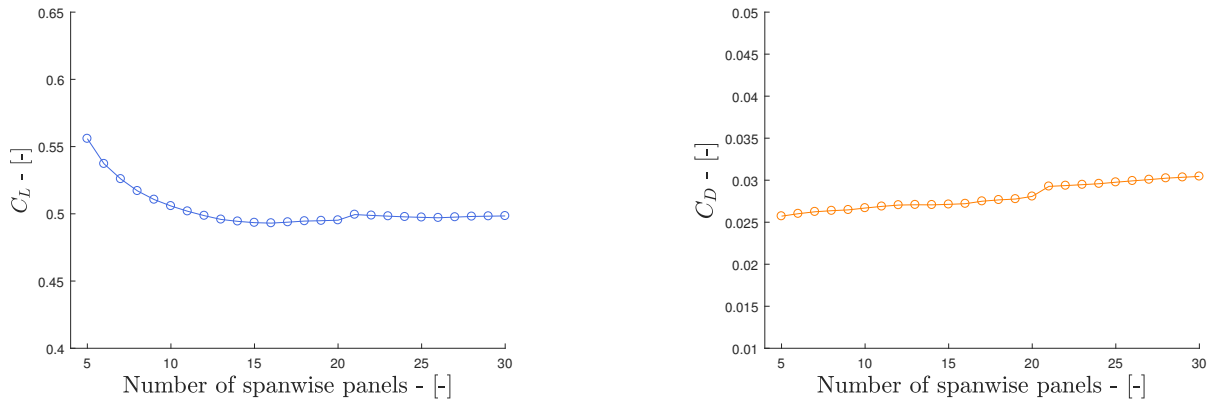

Figure 2.7: Evolution of the lif and drag coefficients with the number of spanwise panels per half-wing, with M = 15 and an AoA of 10 degrees.

Starting from this point, increasing the number of panels leads to a first peak in the value of the lift and drag coefficients. This is explained by the definition of the Biot-Savart law in Eq.(2.5). The expression of the latter contains the distance between the segment and the point on the denominator, and thus have a singularity when this distance becomes equal to zero. Since a growth rate is applied in the spanwise direction, the collocation points and vortex segment are the closest at the tip, and their spacing decreases as the number of panels increases. When the number of panels becomes too high, the induced velocity gets huge and it results in a loss of accuracy in the computed loads. This phenomenon is visible in Fig.2.8, where the shed panels at the tip diverge on (b).

(a) (b)

Figure 2.8: 3D view of the sail and its wake in *Matlab* for an AoA of 10 degrees with M = 15 and (a) N = 15, (b) N=25.

To avoid it, a spanwise division in less than 20 panels is preferable, and eventually, a number of 15 panels will be chosen for the half-wing, taking into account the CPU time that increases exponentially, as shown in Fig.2.9.

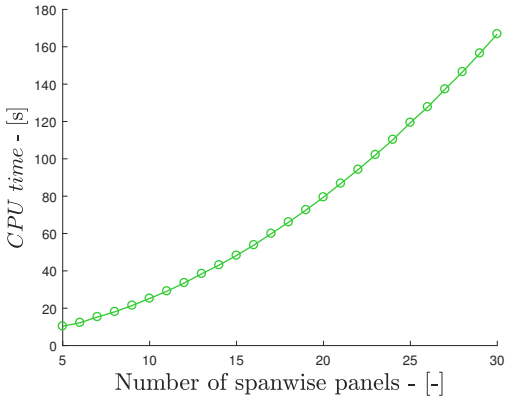

Figure 2.9: Evolution of the CPU time with the number of spanwise panels per half-wing, with M = 15.

4.4 Number of chordwise panels

The number of division in the chordwise direction is now addressed. The evolution of the aerodynamic coefficient is plotted in Fig.2.10. If the drag coefficient converges quickly, the lift coefficient is slowly decreasing as the number of chordwise panels is increasing. It actually decreases linearly and never converges, until eventually the VLM code fails due to the too large amount of panels and gives incoherent values. The choice is then based on the drag's convergence and on the CPU time, taking 20 divisions per half-wing as a good compromise.

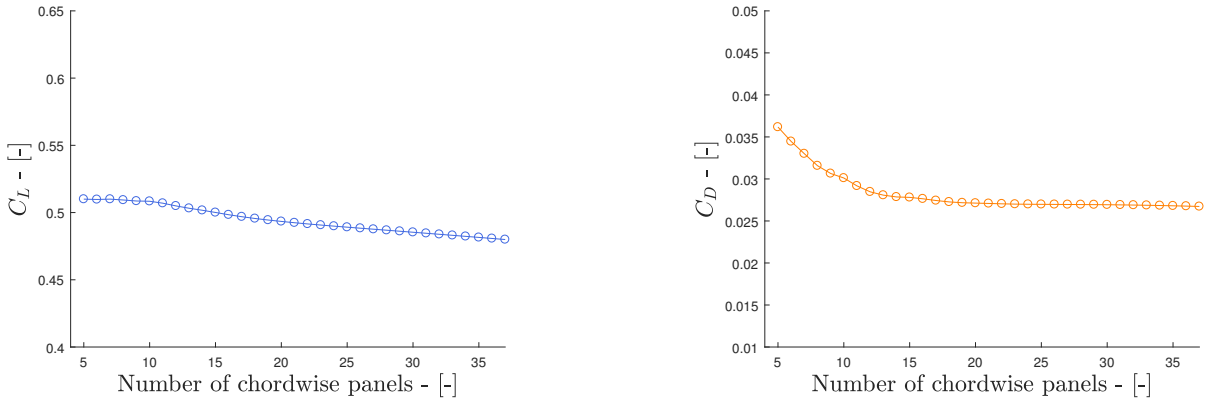

Figure 2.10: Evolution of the lif and drag coefficients with the number of chordwise panels per half-wing, with N = 15 and an AoA of 10 degrees.

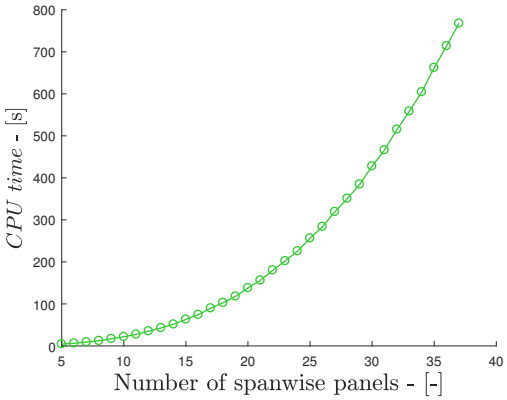

Figure 2.11: Evolution of the CPU time with the number of chordwise panels, with N = 15.

4.5 Wake model

As mentioned in the VLM description, the wake influence can be modelled using either a free or a flat wake model. As a reminder, the free wake model considers the wake roll-up by moving the shed vortex rings with the local velocity. The wake suit then better the reality and the results are usually more accurate. The drawback is that the computation of the wake's position at each iteration is time-consuming. In contrast, the flat wake model simply propagates the shed vortex rings with the free stream, so the wake constitutes a flat path. Both models are represented in Fig.2.12.

(a) (b)

Figure 2.12: Shedding process of the VLM for the free (a) and flat (b) wake models, at an angle of attack of 10 degrees.

The choice is then a trade-off between results accuracy and time cost. The CPU time belonging to each wake model, for M=15 and N=20 is shown in Tab.2. If the flat wake model is nearly 3 times faster the free wake model, both magnitudes are acceptable.

Wake model	CPU time - [s]
Flat wake	26.5
Free wake	65.2

Table 2: Variation of the aerodynamic coefficients and CPU time of the sail with the domain's length.

In principle, the free wake model should also provide in our case the most reliable results and is then preferred in the following sections since they aim to compare the results provided by the vortex lattice method to real physical ones. This statement will be proved in the next chapter when comparing both models with the wind tunnel model.

5 Results

5.1 Aerodynamic coefficients

Finally, simulations on the chosen configuration are performed for angles of attack ranging from 0 to 90 degrees. Those angles correspond to the dimetrodon's possible positions with respect to the wind. The results are presented in Fig.2.13. The behaviour at low angles of attack seems coherent for the lift, especially by looking closer on (a), where a linear evolution can be observed. The same conclusion can be deduced for the drag on (b) and its classic quadratic shape. Those are the typical curves for a symmetric wing.

However, the behaviour at high angle of attack is less coherent, especially for the drag coefficient, which falls as the angle reaches 90 degrees, yet meaning that the sail is completely

perpendicular to the free stream and then generating a significant amount of drag. It is not a surprise since, as mentioned in the potential flow description, the VLM does not represent flow separation and is then not trustworthy for the prediction of aerodynamic loads at high angles of attack.

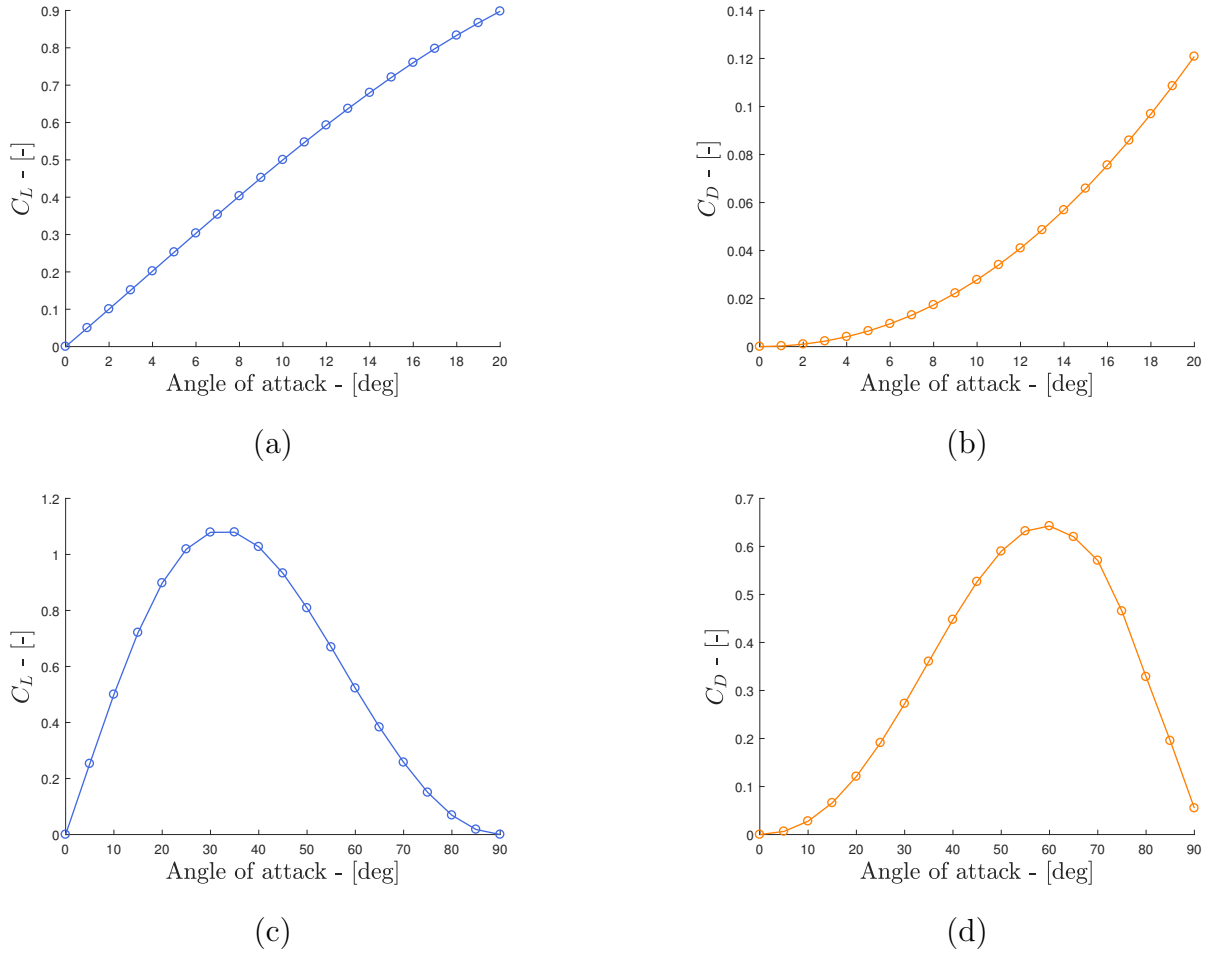

Figure 2.13: Evolution of the lift and drag coefficients for AoAs ranging (a)-(b) from 0 to 20 [deg] and (c)-(d) from 0 to 90 [deg]', with M=20 and N=15.

5.2 Lift distribution

The lift coefficient distribution, when the sail is exposed at an angle of attack of 20 degrees, is depicted in Fig.2.14. The spanwise distribution is quite typical, with a gradual decrease from the root to the tip of the sail. The chordwise lift is characterized by a peak at the proximity of the leading edge represented at the 1st row of panels before a fast decrease as the coefficient of the second row of panels is already way smaller. This distribution pattern remains more or less unchanged for every other angle of attack, only the value of the lift coefficient changes.

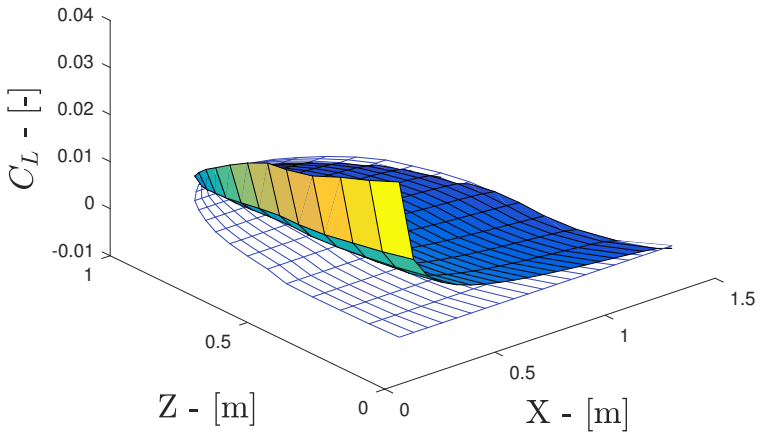

Figure 2.14: Lift distribution of the VLM model at an AoA of 20 degrees.

If the results seem logical at low and medium angles of attack, validation is needed to acknowledge this model's limits and go further with the aerodynamic stability study of the dimetrodon. This will be done in the next chapter.

Chapter 3

Wind tunnel testing

As a reminder, the VLM is a potential method and therefore do not account for several concepts, such as friction drag or flow separation. It is then important to verify the results obtained previously by comparing them with values coming from another method, ideally considering those viscous phenomena. The best way to check numerical results is to compare them with a physical model submitted to real conditions. Since the University of Liège possesses a state-of-the-art wind tunnel, this experiment has been made possible.

1 Wind tunnel description

The test section of the wind tunnel used for the test campaign is 2.5 [m] width, 1.8 [m] high and 13.5 [m] long. The vein is equipped with a rotating test table so that different angles of attack can be applied to the tested model. Wind speed up to 60 [m/s] can be investigated [4]. The measurements are performed with the *ATI Omega160* transducer [5]. The latter computes with high precision the forces and moments in the 3 directions. The results are given respectively in [N] and in [N·m]. A scheme of the ULg wind tunnel facility is represented in Fig.3.1.

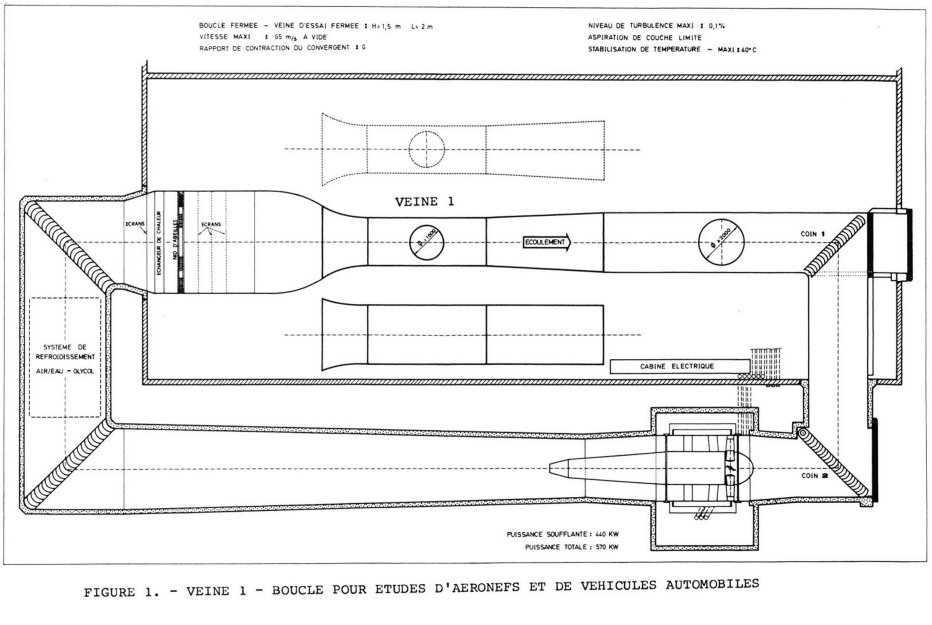

FIGURE 1. - VEINE 1 - BOUCLE POUR ETUDES D'AERONEFS ET DE VEHICULES AUTOMOBILES

Figure 3.1: ULg wind tunnel facility.

2 Model configuration

To make a comparison between the wind tunnel and the VLM relevant, it is important to keep the same shape. The physical model will then follow the sail geometry chosen in chapter 2.

2.1 Sail sizing

Knowing the wind tunnel vein's dimensions, it is essential to choose wisely the size of the model to avoid blocking. This phenomenon happens when the surface of the experimental device is large regarding the tunnel section, causing a part of the upstream flow to block. In that case, the free stream is affected and the results are corrupted.

The blocking ratio is defined as the ratio between the blocking surface and the vein's surface. A maximum limit of 6% is considered acceptable to ensure a successful experiment [6]. Since the area of the wind tunnel section used is 4.5 [m^2], the maximum exposed surface of the sail, i.e. when the angle of attack is equal to 90 degrees, should be below 0.27 [m^2]. When fitting the studied form in a square with an area of 0.25 [m^2] (and sides of 0.5 [m]), its surface reaches 0.136 [m^2]. The blocking ratio is then half the threshold (3.02 %), giving a comfortable safety margin, given that the support will also obstruct the flow. The retained wind tunnel model is then 0.5 meter wide and 0.384 meter high, as pictured in Fig.3.2.

Figure 3.2: Wind tunnel model of the sail on its support in the test vein, at an angle of attack of 90 degrees.

The sail used for the following tests is built on a wood plate. This material is easy to manufacture and is strong enough to withstand the forces that it will face without deformation nor failure. Even though the VLM considers the sail as an infinitely thin plate, it is impossible to create a physical model with no thickness. In this case, the wood plate is 1.2 [cm] thick, giving a length/thickness ratio of less than 3%, which is judged acceptable.

2.2 Support design

Now that the dorsal fin is designed, its configuration in the wind tunnel has to be determined. Several constraints have to be considered to obtain results as reliable as possible.

First, the sail has to be firmly attached to the transducer, which is a cylinder of 156.5 [mm] diameter. This is achieved by putting the fin between two beams, that will, in turn, be attached to the sensor via 4 bolts. The latter is placed at the top of a leg of 40 [cm] so that the sail stand above the boundary layer developed by the wind tunnel floor (which is about 10 [cm] high) and keep the incoming flow as uniform as possible. This first mounting step is shown in Fig.3.3.

Figure 3.3: View of the first step of the assembly, with the sail fixed to the transducer.

The problem of this assembly is that the two beams, considered as bluff bodies, induce vortices that disturb the airflow around the fin, and compromise the collected data. The second step is then to build a "table" to ensure, once again, an incoming airflow as uniform as possible. The transducer and the fixing system are dissimulated under the table so they don't have any influence on the flow seen by the studied shape. If the gap between the "table" and the first assembly has to be small to avoid perturbations, it also essential to prevent any contact between those two in order to avoid unwanted loads during the measurements. Note that the two front legs are actually two plates placed in a "V" configuration, so that they act as deflectors and protect the sensor from unwanted loads coming along with the airflow, as shown in Fig3.4.

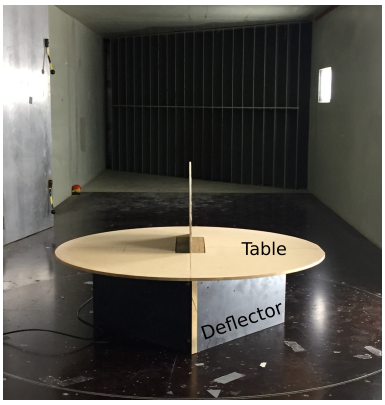

Figure 3.4: Front view of the final assembly.

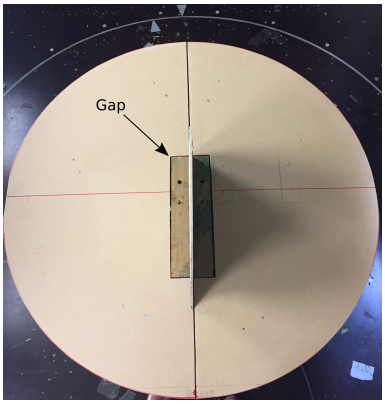

Figure 3.5: Top view of the final assembly.

2.3 Measurement methodology

As mentioned previously, the transducer is used to measure the moments and forces applied to the experimental device for each test condition in the three directions. The coordinates system attached to the sensor and then to our plate is described in Fig.3.6. The *ATI Omega160* is fixed at the wing's quarter chord, where the aerodynamic forces are applied. The X-direction is parallel to the sail, the Y-direction is perpendicular and the Z-direction is the vertical one.

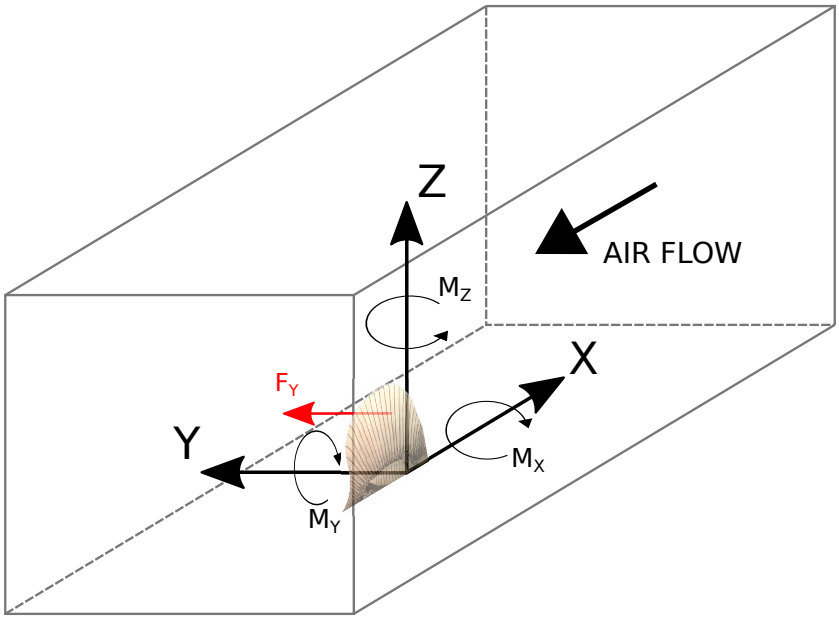

Figure 3.6: Scheme of the coordinates system.

The dimensionless coefficients C_{F_X} and C_{F_Y} are found using the following expressions:

$$C_{F_X} = \frac{2F_X}{S\rho {U_\infty}^2} \tag{3.1}$$

$$C_{F_Y} = \frac{2F_Y}{S\rho {U_\infty}^2}, \tag{3.2}$$

with F_X and F_Y the forces applied along the X and Y directions, S the sail's surface (0.136 [m^2]), ρ the air density measured the day of the tests (1.2293 [kg/m^3]) and U_∞ the airspeed.

Knowing that the lift and drag are respectively perpendicular and parallel to the free stream, their coefficients C_L and C_D can then be derived using the following expressions:

$$C_L = C_{F_Y}\cos(\alpha) - C_{F_X}\sin(\alpha) \tag{3.3}$$
$$C_D = C_{F_Y}\sin(\alpha) + C_{F_X}\cos(\alpha), \tag{3.4}$$

with α the angle of attack.

Once the airflow set to the desired speed, the plate is positioned to the tested angle of attack thanks to the rotary plate on which the whole system is fixed. When ready, a range of measures is registered, for 30 seconds. Since 50 measures are recorded in one second, the test will eventually provide a large sample that allows making an average on the captured values. Indeed, the forces and moments fluctuate during the test, due to the airflow fluctuations and the vibrations of the plate.

3 Sensor corrector term

The transducer used being extremely sensitive, some unwanted effects due to various sources can make the results irrelevant. The first is the thermal expansion of some pieces inside the sensor, coming from the temperature rise occurring when it is turned on. It causes internal stresses that affect significantly the data collected. This problem is easily avoided by waiting a few minutes so that the temperature within the device is stable.

The second problem is happening during loading and concerns an unexpected relation between the value of the moments and the forces computed. Indeed, when the sensor is under loading, the moments sustained seem to create internal stresses that will add to the computed forces. This is why it is common to apply a correction to the results. The correction term is calculated by applying several pure moments, using weights of 10 [N] placed at several distances from the transducer on the 3 axes of the model at rest, and seeing their influence on the forces computed. Note that the correction term was not calculated for the force along the vertical (Z) axis since it is negligible and not of interest in this thesis.

As shown by Fig.3.7, Fig.3.8 and Fig.3.9, the forces indeed vary with the different moments applied, and in a relatively linear way, since a polynomial of the first degree can be efficiently fitted to the data. The polynomial coefficients are calculated and for each experiment, the value of the computed force F_0 will be corrected according to the value of the three moments. The corrected value F_C will then be equal to

$$F_C = F_0 + A_{X_0} + A_{X_1}M_X + A_{Y_0} + A_{Y_1}M_Y + A_{Z_0} + A_{Z_1}M_Z, \tag{3.5}$$

with $A_{X_0}, A_{X_1}, A_{Y_0}, A_{Y_1}, A_{Z_0}$ and A_{Z_1} the coefficients of the 3 polynomials computed in the correction tests. This method will be applied to the forces in the X and Y directions, F_X and F_Y.

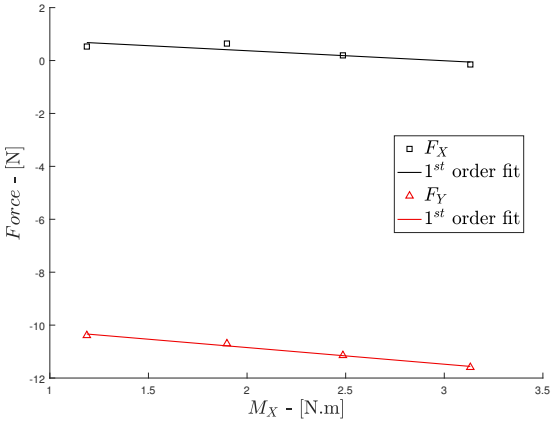

Figure 3.7: Variation of the force along the X and Y axis with the moment M_X.

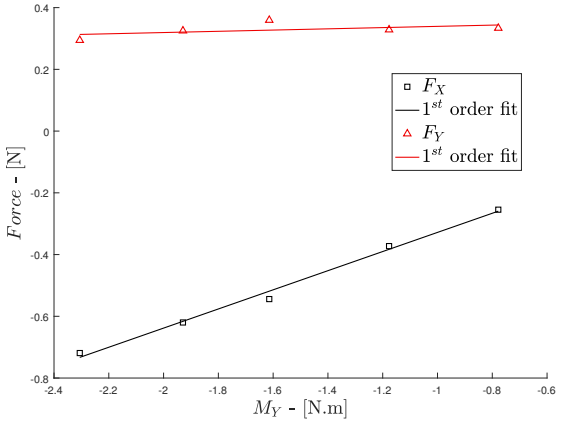

Figure 3.8: Variation of the force along the X and Y axis with the moment M_Y.

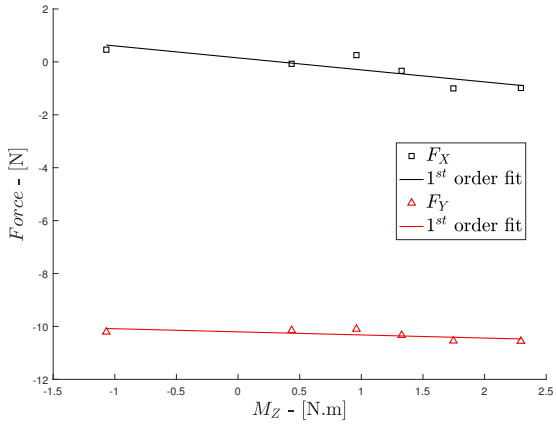

Figure 3.9: Variation of the force along the X and Y axis with the moment M_Z.

4 Reynolds number effect

When reproducing a wind-structure interaction, the Reynolds number effects have to be considered. The Reynolds number parameter is defined as

$$Re = \frac{UL}{\nu}, \tag{3.6}$$

where U is the airspeed in [m/s], L a characteristic linear dimension [m] and ν is the kinematic viscosity of the fluid. This is actually the ratio between the inertial and the viscous forces.

If the aerodynamic coefficients should be independent on the wind speed, this is not the case at low airspeeds/Reynolds number, as shown in Fig.3.10. At first, the value of the aerodynamic coefficients evolve significantly with the wind speed. It then converges as the speed of the flow increases, meaning that the viscous effects become negligible. The tests have been performed at a speed of 15 [m/s], giving satisfying results. Repeating the experiments at higher airspeeds would, according to the graphs, increase the accuracy and the reliability of the results.

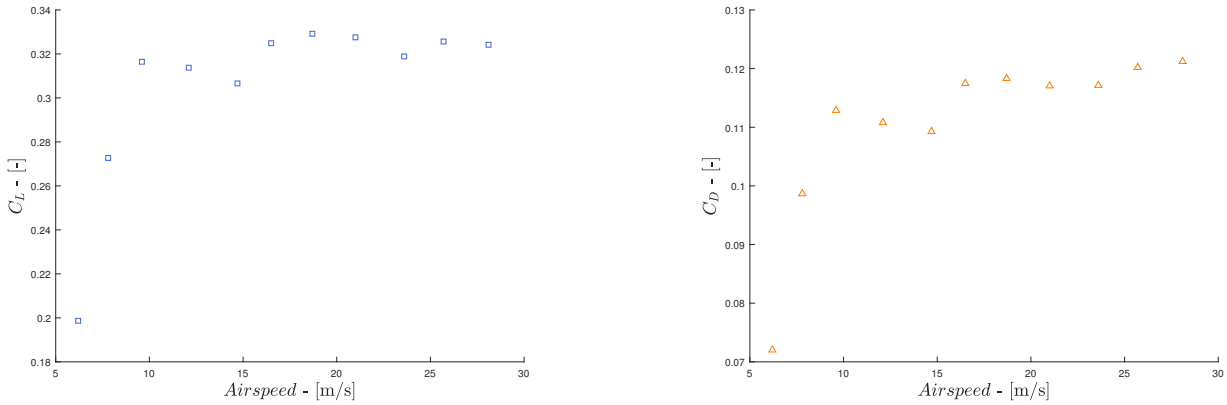

Figure 3.10: Variation of the lift and drag coefficients with the airspeed, at an AoA of 10 degrees.

5 Results

Aerodynamic coefficients at small angles of attack

The value of the coefficients is first obtained for angles of attack varying from 0 to 20 degrees. As a reminder, the physical model is in a viscous flow and thus has to face flow separation. This phenomenon should happen within this range of small angles of attack. In order to capture it as accurately as possible, measures every two angles are being registered.

It is important to note that if the inviscid flows is a good approximation for the lift, it is not really the case for the drag [7]. The reason is that, besides separation, a physical model is also subject to other viscous effects, such as friction drag and turbulence. Knowing that the physical model is 1.2 cm thick, it produces inevitably a certain amount of drag at 0 angle of attack.

As shown by Fig.3.11, featuring the mean value of the lift coefficient given by the sensor with its mean square error, the results obtained by the wind tunnel test match pretty well the ones computed by the VLM, for the ten first measures. When increasing the angle of attack beyond ten degrees, the curves begin to diverge. The most likely cause is that the physical model is dealing with the expected flow separation as the angle of attack of the thin plate increases, which is not handled by the VLM, working with the assumption of inviscid flow. Note that the free wake model better matches the experimental results for the biggest angles, as expected with the increasing wake roll-up.

The drag coefficient found by the wind tunnel model is, as expected, significantly higher than the one calculated numerically. The initial offset corresponds to the drag coefficient at 0 AoA, C_{D_0}. The latter is approximately equal to 0.05 according to the tests. To better compare the two curves, this value is added to the curve obtained by the VLM on Fig.3.12. The small decrease in the drag coefficient for the 4 first AoAs is due to the corrector terms which scale corresponds to the small initial increase in drag at small angles of attack. As before, the curves match relatively well for the first ten AoAs. Beyond those angles, the wind tunnel curve does no longer follow the tendency of the curves given by the VLM. Once again, for the largest AoAs, the free wake model gives the most relevant results.

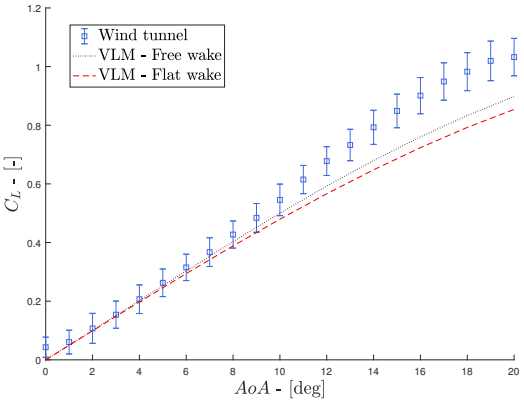

Figure 3.11: Variation of the lift coefficient with the AoA, for the wind tunnel and VLM models.

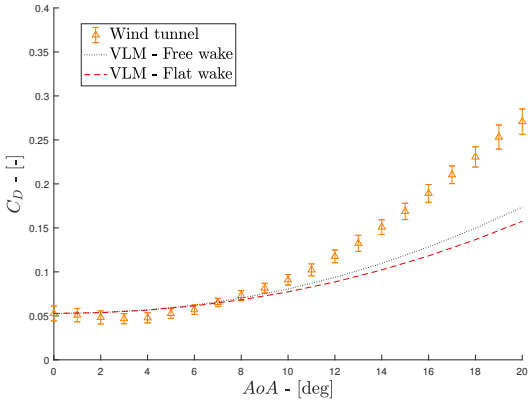

Figure 3.12: Variation of the drag coefficient on a small range of AoA, for the wind tunnel and VLM models.

5.1 Aerodynamic coefficients at high angles of attack

The experiment is then repeated for a bigger range of angles of attack, going up to 90 degrees. The Fig.3.13 shows that the sail completely stalls at an angle of approximately 20 degrees. The results given by the VLM model beyond this value start to diverge significantly. It get worse above 50 degrees, especially when looking at the evolution of the drag coefficient in Fig.3.14, where the drag tends to zero as the plate tends to be perpendicular to the flow. The results given by the VLM should then be treated carefully at high angles of attack.

A second observation can be made by looking closer at the variation of the coefficients' root mean square error with the angle of attack. The highest fluctuations of the lift happen after the stall, involving turbulence and then vibrations. The drag's fluctuation is increasing with the angle of attack and gets its highest value as the plate becomes perpendicular to the stream, leading to high drag magnitude and thus high vibrations.

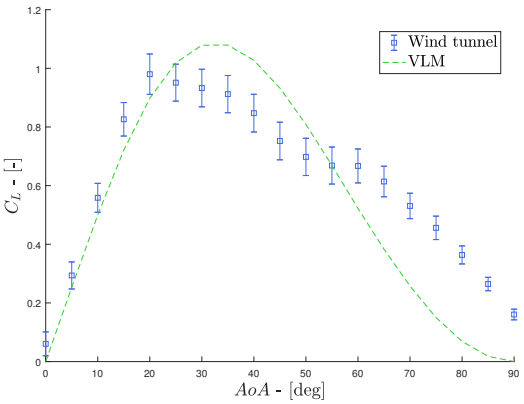

Figure 3.13: Variation of the lift coefficient with angles of attack varying from 0 to 90 degrees, for the wind tunnel and VLM models.

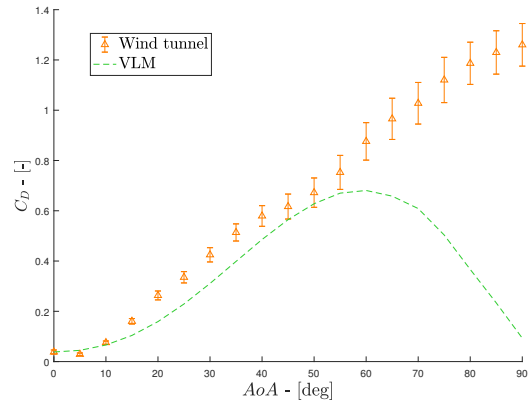

Figure 3.14: Variation of the drag coefficient with angles of attack varying from 0 to 90 degrees, for the wind tunnel and VLM models.

5.2 Overturning force

The force that will cause the dimetrodon to tilt and eventually tip over is the one directed perpendicularly to the animal's sail. It then corresponds to the force captured in the Y-direction F_Y on Fig.3.6 by the sensor. As a reminder, the normal force coefficient C_{F_Y} is linked to the aerodynamic coefficient by:

$$C_{F_Y} = C_L \cos(\alpha) + C_D \sin(\alpha). \tag{3.7}$$

Its coefficient variation with the angle of attack is described in Fig.3.15. Following its definition in Eq.(3.7), the main contribution at small AoAs comes from the lift as it follows the C_L tendency found before. It then remains constant and even decreases as the thin plate stalls. Finally, when the sail reaches approximately 50 degrees, the drag becomes the major contributor and F_Y increases again. The maximum value is then obtained at the maximum angle of attack, meaning that the worst situation for the dimetrodon is to be in the transverse direction with respect to the flow.

The value of the coefficient is then compared to the one obtained by the VLM model in Fig.3.16. It can be seen that the overturning force is pretty well predicted by the VLM, up to an angle of 50 degrees, despite the assumptions of the potential flow theory.

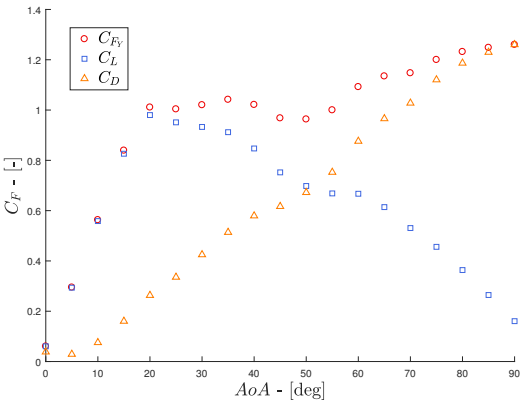

Figure 3.15: Variation of the overturning force coefficient C_{F_Y} with the AoA.

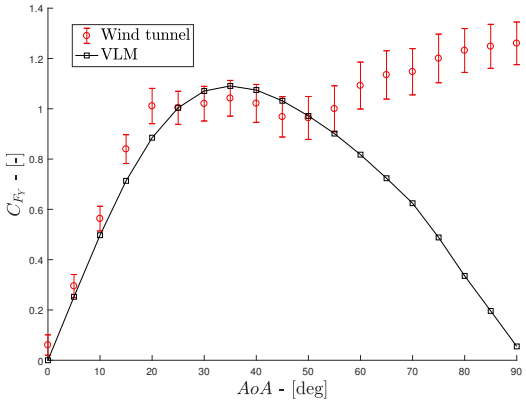

Figure 3.16: Comparison of the C_{F_Y} obtained by the wind tunnel and the VLM model.

5.3 Moments

The evolution of the moments coefficients along the X, Y and Z axis (respectively the rolling, pitching and yawing moments) is described by Fig.3.17. As a reminder, their definition is the flollowing:

$$C_M = \frac{2M}{S\rho {U_\infty}^2 c}, \tag{3.8}$$

where c is the model's chord, here equal to 0.5 [m]. Those are computed by the *ATI Omega160* which, as a reminder, is placed at the quarter chord of the sail's root. Mathematically, the moments M_X, M_Y and M_Z are respectively defined by

$$M_X = F_Y \times Z_{CP}, \tag{3.9}$$
$$M_Y = F_X \times Z_{CP}, \tag{3.10}$$
$$M_Z = F_Y \times X_{CP}, \tag{3.11}$$

where F_Y and F_X are the force components and X_{CP} and Z_{CP} describe the position of the centre of pressure (CP) **with respect to the sensor**. The latter corresponds to the point around which the aerodynamic moments vanishes. Note that the Z component being negligible, it is not taken into account in the calculations for the sake of simplicity.

The three moments increase with the angle of attack, and quite significantly for the rolling (M_X) and yawing (M_Z) moments. Since both depend on the spanwise position of the centre of pressure, it can be deduced than the force in the Y-direction is globally higher than the one in the X-direction. The low value of the pitching moments M_Y comes from the low value of F_X. Finally, the maximum value of all three coefficients is found when the sail is perpendicular to the flow. Knowing the influence of the moments on the forces computed by the sensor, the corrector terms given by Eq.(3.5) are indeed needed.

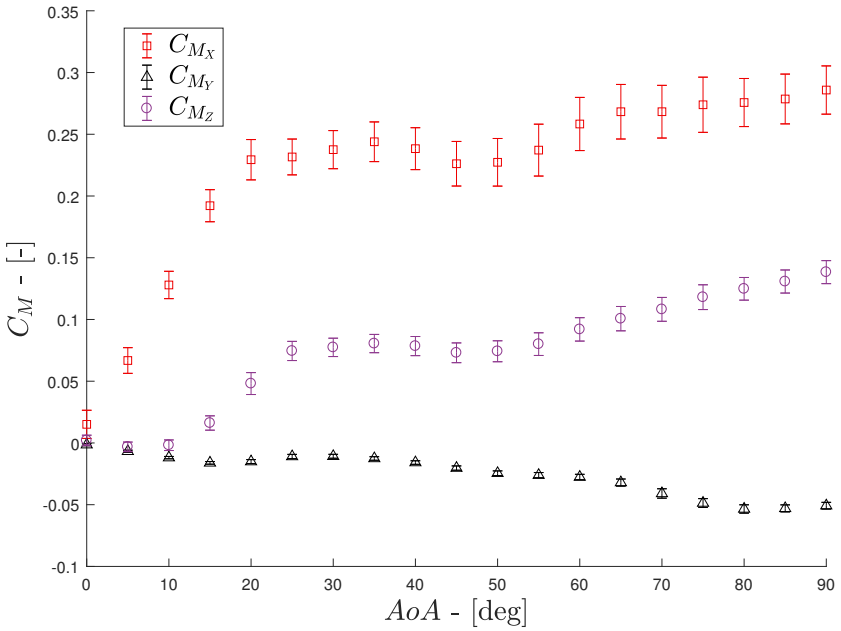

Figure 3.17: Variation of the moment coefficient along the X, Y and Z axis with the angle of attack.

5.4 Centre of pressure

Introduced before, the centre of pressure is, in fact, the geometrical point where the resultant load effectively acts on the body. Its position on the sail is then of interest when evaluating the dimetrodon's stability. Knowing that the transducer computes the moments as well as the forces in the 3 directions, it is then possible to retrieve the position of the centre of pressure of the sail at each angle of attack using Eq.(3.9) and (3.11). Since the sensor is placed at the quarter chord, the corresponding length (here 0.125 [m]) is added to X_{CP} to obtain the coordinates of the centre of pressure with respect to the sail's leading edge.

It is possible to compare the obtained value with the VLM, which provides the lift distribution on the collocation points, allowing the geometrical position $(X_{CP}, Z_{CP})_{VLM}$ to be computed via:

$$X_{CP} = \frac{\sum X_i L_i}{L_{tot}}, \; Z_{CP} = \frac{\sum Z_i L_i}{L_{tot}}, \qquad i = 1...M \times N \tag{3.12}$$

where X_i and Z_i are the coordinates of the collocation point i with respect to the leading edge, L_i its associated lift and L_{tot} the total lift generated by the sail.

The centre of pressure position obtained by the wind tunnel and the VLM models (non-dimentionalized by their respective chord length) are displayed in Fig.3.18 and 3.19. If the chordwise position X_{CP} is initially close to the quarter chord for both models, it diverges starting from 10 degrees as the value given by the VLM remain stable when the one given by the wind tunnel increases. The main explanation is that, based on the previous results, the flow seems to detach significantly starting from 10 degrees, leading to a big variation in the chordwise position of the centre of pressure. Starting from 45 degrees, the X-coordinate given by the VLM starts to have important variations and eventually reaches important negatives values for the last two values, which are discarded for the sake of clarity.

The spanwise position of the centre of pressure Z_{CP} is in contrast relatively close and constant for both models, for the first 50 values. Then, as before, the curve given by the VLM starts to vary quite significantly and once again, the 4 last figures are largely negatives and discarded.

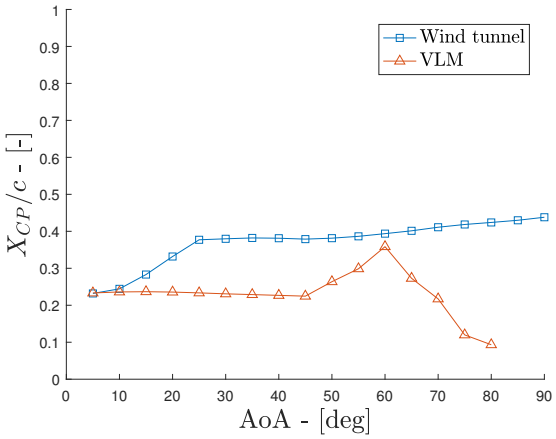

Figure 3.18: Variation of the X position of the center of pressure with the AoA, for the wind tunnel and VLM models.

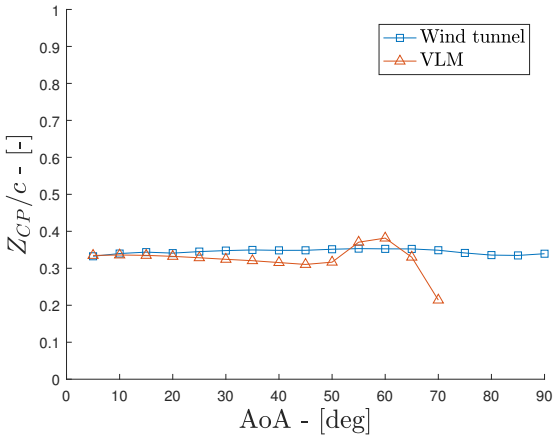

Figure 3.19: Variation of the X position of the center of pressure with the AoA, for the wind tunnel and VLM models.

To better visualise the sail's centre of pressure, its position is displayed in Fig.3.20 for both models at an angle of attack of 10 degrees. It can be observed that both predictions are really close to the quarter chord at this small angle of attack. The position at 90 degrees for the wind tunnel is also represented, to reflect its tendency to move to the centre of the sail when the latter is perpendicular to the flow, which is quite intuitive.

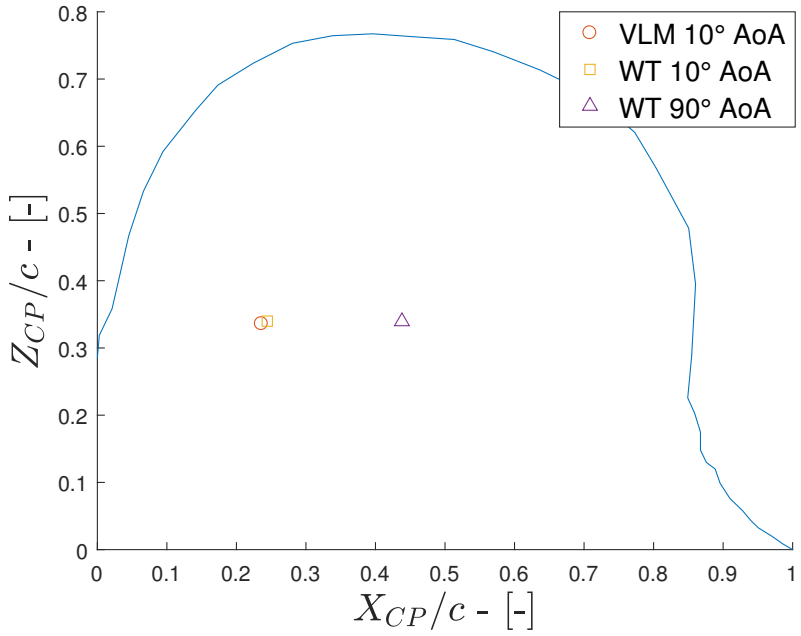

Figure 3.20: Scheme of the sail and its centre of pressure prediction by the wind tunnel and VLM models.

In conclusion, and based on the different observations made throughout this section, it looks like the VLM model is very efficient at very low angles of attack (< 10 [deg]), then begins to lose precision and eventually fails at large angle of attack (> 50 [deg]). This brings to light the limits of the vortex lattice method, which will be considered in the later stages of this thesis when the VLM will be associated with a finite element model.

5.5 Flow separation visualisation

Too validate the previous estimation of the separation angle of attack, a special test is performed in order to observe visually the separation on the sail. To do so, several cotton strings are stuck to the sail in the spanwise and chordwise direction.

At zero angle of attack, the flow on the plate is laminar and all the strings are aligned with the freestream. When applying an angle of attack of 5 degrees, the Fig.3.21 shows that the first two string columns (in red) are not aligned anymore, due to the formation of a small separation bubble at the leading edge. This phenomenon is enhanced by the non-smooth, square leading edge of the plate. This bubble grows as the angle of attack increases, and at an angle of 15 degrees, only the last two columns are still straight, while all the others are moving in every direction. Eventually, all the strings are disturbed at an angle of attack of 20 degrees. Those observations confirm the previous results, i.e. that the plate is completely stalled when its angle of attack exceeds 20 degrees.

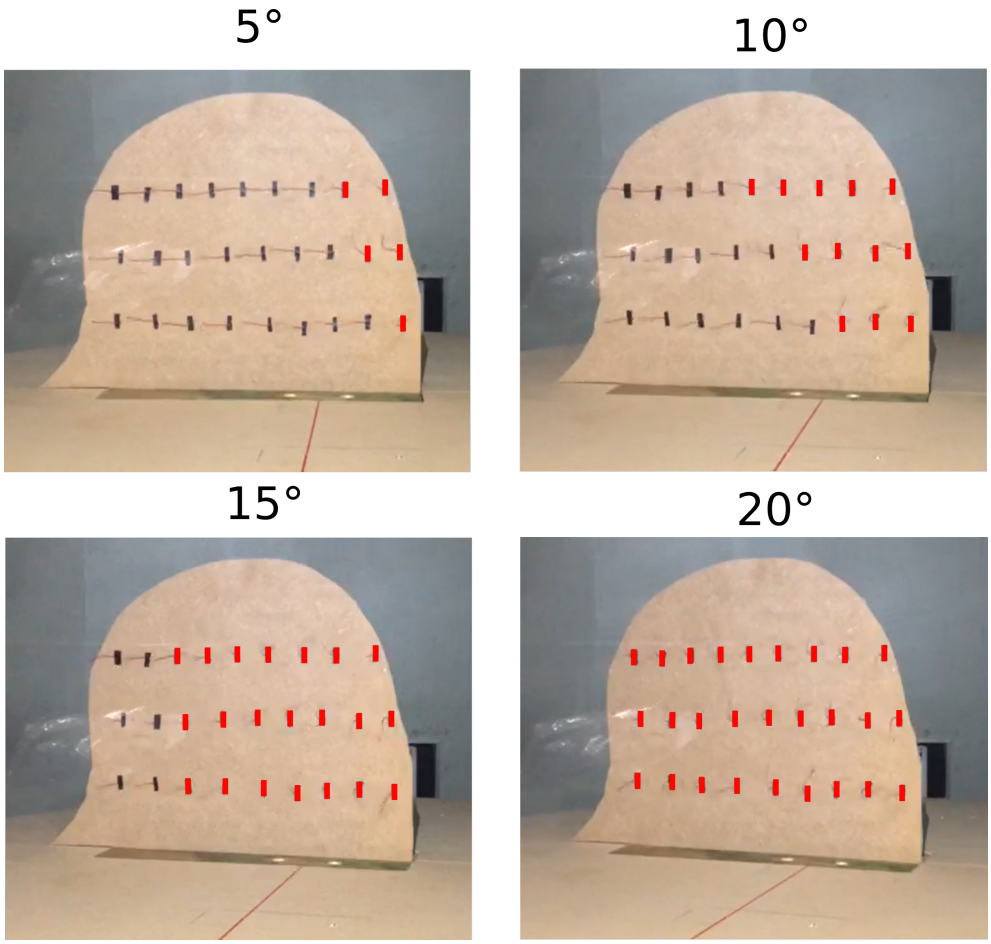

Figure 3.21: Visualisation of the flow separation at angles of attack of 5, 10, 15 and 20 degrees.

Chapter 4

Finite element analysis

Now that the evolution of the aerodynamic coefficients is known, the response of the sail to the resulting aerodynamic loads is considered. Until now, the plate was assumed infinitely rigid. In reality, the dimetrodon's dorsal bones are flexible and then deforms when submitted to substantial loads. This shape modification may affect the aerodynamics of the animal and thus its stability. The finite element analysis is here implemented in *Matlab*.

1 Structure modelling

The model once again follows the contours of the selected skeleton in chapter 2. The bones are modelled as 3D beams, considered as a good approximation in the case of elongated shapes [8]. Since the dimetrodon could seize up to 2 meters, the geometry will correspond to a sail of 1 meter high and 1.3 meters wide, considering a full-grown specimen. The model is composed of 37 bones (counted from the representative geometry). The bones are assumed to have a constant circular cross-section along the dorsal, with a diameter of 2 [cm]. Since no reliable values of the bone properties of pelycosaurs could be found on the literature, the parameters are taken from a common human bone and are the following [9]:

- Density:
$$\rho = 2000 \text{ [kg/m}^3\text{]}, \tag{4.1}$$
- Young's modulus:
$$E = 12 \text{ [GPa]}, \tag{4.2}$$
- Poisson's ratio:
$$\nu = 0.3 \text{ [-]}. \tag{4.3}$$

The beams in the model are assumed to be rigidly clamped to the chord root, representing the backbone. This is the only boundary condition considered. A view of the finite element model in *Matlab* is shown in Fig.4.1.

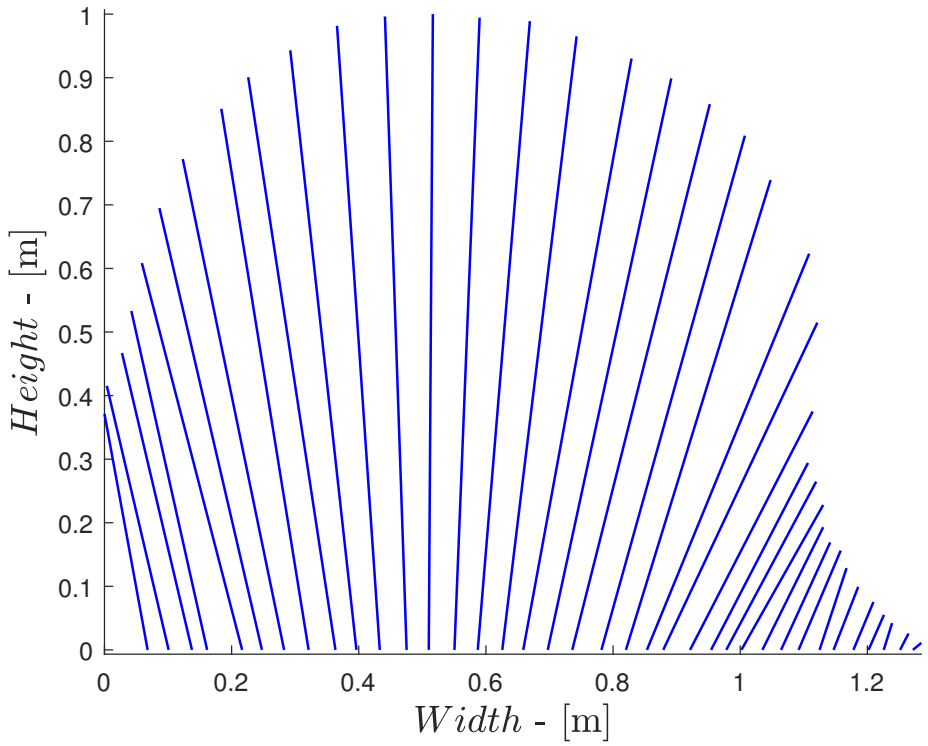

Figure 4.1: Modelling of the sail's structure in *Matlab*

The whole model relies on the simple linear equation

$$\mathbf{K}_S \mathbf{q} = \mathbf{F}_l, \tag{4.4}$$

where $\mathbf{K}_S$ is the structural stiffness matrix, $\mathbf{q}$ the degrees-of-freedom and $\mathbf{F}_l$ the applied loads (here the aerodynamic loads computed by the VLM model).

1.1 Stiffness matrix

Using the finite element method (FEM), the beams are divided into elements and the structural stiffness matrix is built for each one of them using the following equation:

$$\mathbf{K}_{eS} = \mathbf{T}_e^T \mathbf{K}_{eL} \mathbf{T}_e. \tag{4.5}$$

As a reminder, the degrees-of-freedom in a 3D beam element relying two nodes are:

$$\mathbf{q}_{el}^T = [\ u_1 \quad v_1 \quad w_1 \quad \psi_{x_1} \quad \psi_{y_1} \quad \psi_{z_1} \quad u_2 \quad v_2 \quad w_2 \quad \psi_{x_2} \quad \psi_{y_2} \quad \psi_{z_2}\ ] \tag{4.6}$$

with u, v and w the displacements in the 3 directions, and ψ_x, ψ_y, ψ_z the 3 components of rotation.

The elementary stiffness matrix is defined as

$$\mathbf{K}_{el} = \begin{bmatrix}
0 & \frac{12EI_z}{l^3} & & & & & & & & & & \\
0 & 0 & \frac{12EI_y}{l^3} & & & & & & & & & \\
0 & 0 & 0 & \frac{GJ_x}{l} & & & & & & & & \\
0 & 0 & \frac{-6EI_y}{l^2} & 0 & \frac{4EI_y}{l} & & & & & & & \\
0 & \frac{6EI_z}{l^2} & 0 & 0 & 0 & \frac{4EI_z}{l} & & & & & & \\
\frac{-EA}{l} & 0 & 0 & 0 & 0 & 0 & \frac{EA}{l} & & & & & \\
0 & \frac{-12EI_z}{l^3} & 0 & 0 & 0 & \frac{-6EI_z}{l^2} & 0 & \frac{12EI_z}{l^3} & & & & \\
0 & 0 & \frac{-12EI_y}{l^3} & 0 & \frac{6EI_y}{l^2} & 0 & 0 & 0 & \frac{12EI_y}{l^3} & & & \\
0 & 0 & 0 & \frac{-GJ_x}{l} & 0 & 0 & 0 & 0 & 0 & \frac{GJ_x}{l} & & \\
0 & 0 & \frac{-6EI_y}{l^2} & 0 & \frac{2EI_y}{l} & 0 & 0 & 0 & \frac{6EI_y}{l^2} & 0 & \frac{4EI_y}{l} & \\
0 & \frac{6EI_z}{l^2} & 0 & 0 & 0 & \frac{2EI_z}{l} & 0 & \frac{-6EI_z}{l^2} & 0 & 0 & 0 & \frac{4EI_z}{l}
\end{bmatrix}, \quad (4.7)$$

with

- l the length of the element,
- A the cross-section area,
- E the Young's modulus,
- G the shear modulus,
- J_x torsional constant of the cross-section,
- I_y the second moment of area about the axis y,
- I_z the second moment of area about the axis z,

Moreover, in Eq.(4.5), $\mathbf{T}_e$ is :

$$\mathbf{T}_e = \begin{bmatrix} \mathbf{R}_e & 0 & 0 & 0 \\ 0 & \mathbf{R}_e & 0 & 0 \\ 0 & 0 & \mathbf{R}_e & 0 \\ 0 & 0 & 0 & \mathbf{R}_e \end{bmatrix}, \quad (4.8)$$

with $\mathbf{R}_e$ the rotation operator defined by the following scalar products:

$$\begin{Bmatrix} x_i \\ y_i \\ z_i \end{Bmatrix} = \begin{bmatrix} \vec{e}_X \bullet \vec{e}_x & \vec{e}_Y \bullet \vec{e}_x & \vec{e}_Z \bullet \vec{e}_x \\ \vec{e}_X \bullet \vec{e}_y & \vec{e}_Y \bullet \vec{e}_y & \vec{e}_Z \bullet \vec{e}_y \\ \vec{e}_X \bullet \vec{e}_z & \vec{e}_Y \bullet \vec{e}_z & \vec{e}_Z \bullet \vec{e}_z \end{bmatrix} \begin{Bmatrix} X_i \\ Y_i \\ Z_i \end{Bmatrix} = \mathbf{R}_e \begin{Bmatrix} X_i \\ Y_i \\ Z_i \end{Bmatrix}, \quad (4.9)$$

with

$$\vec{e}_x = \left\{ \frac{X_2 - X_1}{l} \quad \frac{Y_2 - Y_1}{l} \quad \frac{Z_2 - Z_1}{l} \right\} \quad (4.10)$$

$$\vec{e}_y = \frac{\vec{d}_3 \times \vec{d}_2}{\|\vec{d}_3 \times \vec{d}_2\|}, \text{ where } \vec{d}_i = \begin{bmatrix} X_i - X_1 & Y_i - Y_1 & Z_i - Z_1 \end{bmatrix} \quad (4.11)$$

$$\vec{e}_z = \vec{e}_x \times \vec{e}_y \quad (4.12)$$

The total structural stiffness matrix $\mathbf{K}_S$ is eventually assembled.

1.2 Aerodynamic loads

Following its definition, the VLM model provides the value of the lift and drag in Newton at each collocation point. This allows to visualize the lift and drag distribution in the chordwise and spanwise direction (Fig.2.14). The loads computed by the VLM are then imported by interpolation from the collocation points to the FEM model's nodes. If the distribution is respected using this approach, the drawback is that the total lift and drag increases with the number of nodes. The force applied to each node is then weighted by a scaling coefficient so that the total lift and drag match the one given by the VLM. Note that the loads are here supposed to be completely transferred from the skin to the bones.

Finally, the contribution of the zero drag coefficient C_{L_0} is dimensionalized and added to the induced drag to obtain the aerodynamic loads vector $\mathbf{F}_l$. The matrix $\mathbf{K}_S$ and the aerodynamic loads vector $\mathbf{F}_l$ being known, the degrees-of-freedom $\mathbf{q}$ can be computed with Eq.(4.4).

1.3 Convergence study

Since the number of finite elements and thus the number of DOF used to model the structure may influence the results, a convergence study has to be performed. The indicator of convergence is the potential energy of the structure when exposed at a wind speed of 20 [m/s] at an AoA of 10 degrees. The latter is defined by

$$V = \frac{1}{2}\mathbf{q}^T\mathbf{K}_S\mathbf{q}, \tag{4.13}$$

and its relative error is mathematically expressed as:

$$\frac{abs(V^{n+1} - V^n)}{V^{n+1}} < 0.02. \tag{4.14}$$

Its evolution with the number of elements per bone is depicted in Fig.4.2. The relative error decreases fastly as the CPU time increases in an exponential manner. Eventually, the number of elements chosen is 12, since the relative error between 12 and 13 beam elements is less than 2% and does not justify an increase in the CPU time.

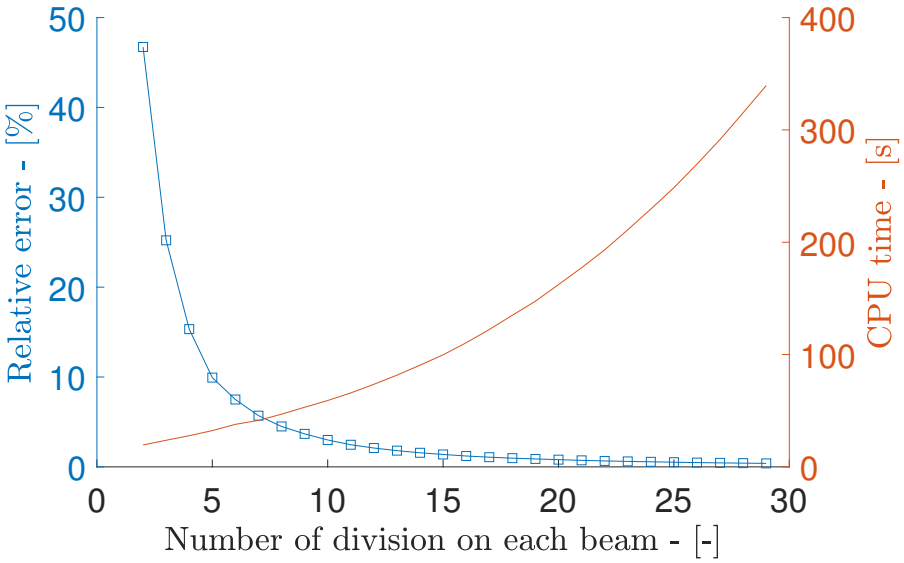

Figure 4.2: Relative error [%] of the potential energy with respect to the number of division on each beam of the structure and the respective CPU time [s].

2 Yield strength

Like every other material, the bone has a yield strength, meaning that when loaded beyond this value, it no longer acts as a spring but deforms permanently and eventually breaks. In the case of the dimetrodon, a too strong aerodynamic loading (at high angles of attack and high wind speeds) may cause the sail to fracture.

The beam's maximum internal stresses in the axial direction are approximated using the following equation:

$$\sigma_{xx} = \frac{M(x)y}{I}, \tag{4.15}$$

where $M(x)$ is the moment experienced at the position x along the beam, y is the beam's radius and I the beam's moment of inertia. Since the system is clamped, the total moment on each beam is found by summing the moments applied by the aerodynamic forces on each node. The value of the maximum stress σ_{max} can then compared to the yield tensile stress σ_y and the ultimate tensile stress σ_u equal respectively to 114 and 133 MPa [9]. It is important to remind that it is a quite gross approximation since the shear stresses are ignored and the values of the bones parameters estimated may be significantly different to the genuine ones.

Chapter 5

FEM and VLM coupling

The FEM and VLM models being implemented, the next step is to couple them so that a flexible model of the sail can be studied in multiple conditions. The number of panels of the VLM model and the number of division per bone of the FEM model found with the convergence tests remains unchanged. The interest is to observe the sail's change in behaviour with the wind speed at various angles of attack. Considering the limits of the VLM, the study is restricted to a maximum angle of 45 degrees. Regarding the wind speed, it is ranging from a "gentle breeze" (5 [m/s]) to a "hurricane force" (more than 32 [m/s]) on Beaufort scale [10]. The join work of 2 large *Matlab* codes induces a big computational cost, and therefore the flat wake model is preferred, given that the resulting loss of accuracy is acceptable. Given the big loss of accuracy when the VLM model is set at large angles of attack, the test is limited to a maximum angle of 45 degrees.

1 Methodology

The coupling process starts by computing the aerodynamic loads for a selected wind speed and angle of attack on the initial model with the vortex lattice method. The displacements are then obtained by applying those loads on the FEM model. A deformed shape is then obtained, and the latter is implemented in the VLM to find the new loads belonging to this new shape. The influence of the new aerodynamic loads on the structure is determined by using the finite element method a second time. If the potential energy of the new shape is close to the previous one, it means that the final deformed shape is determined. Otherwise, new VLM-FEM iterations are performed until a stable configuration is found. A flow chart describing this algorithm is represented in Fig.5.1. The potential energy is thus once again used as the criterion of convergence and the mathematical expression of the relative error is the same as in Eq.(4.14).

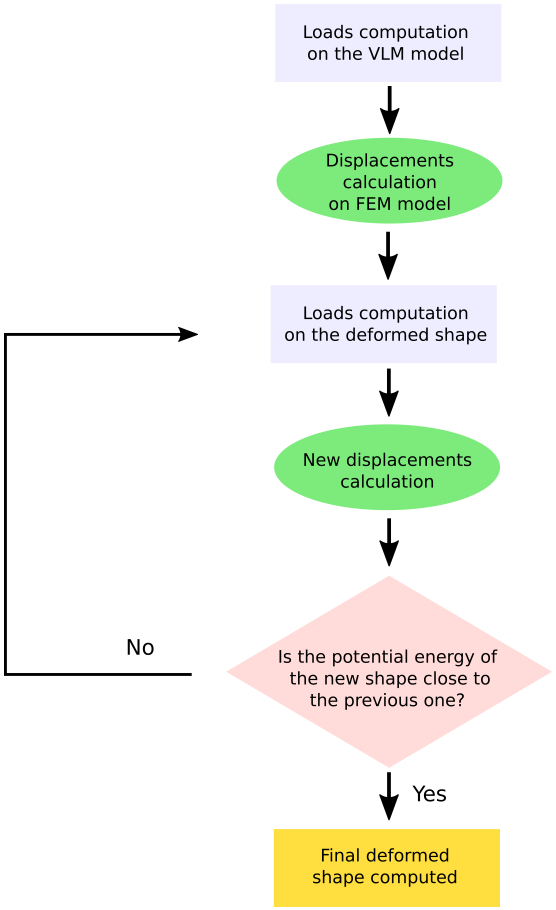

Figure 5.1: Flow chart of the FEM-VLM coupling method.

The relative error of 1% is quickly satisfied at low airspeeds due to the small loads and deformations encountered, as shown by Fig.5.2, where the number of iterations needed for several airspeeds at 45 [deg] of angle of attack is displayed. However, the convergence is longer as the wind speed increases, meaning that the displacements added at each iteration influence the aerodynamic loads of the sail.

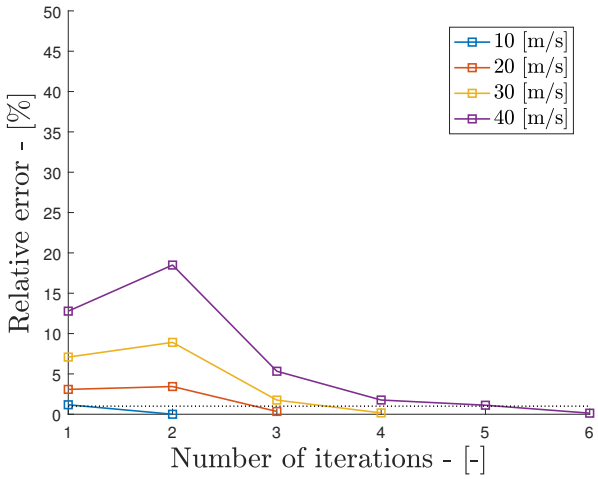

Figure 5.2: Variation of the relative error of the potential energy with the number of iterations, at various airspeeds.

2 Evolution of the stresses

The stresses are computed for each beam, following Eq.(4.15), and the one experiencing the maximum stress is retained. Actually, for every case, the first beam is always the one experiencing the most critical stresses for the 45 first angles of attack due to the load distribution. The results for the 3 largest wind speeds tested are depicted by Fig.5.3. It shows that the maximum stress is far from the yield strength by a comfortable margin since it merely reaches half the limit even at 45 degrees of angles of attack and in case of stormy weather. The relatively small variation of the overturning force F_Y beyond 45 degrees shown by Fig.3.16 in the wind tunnel suggests that the value of the stress should not be significantly higher at 90 degrees. The model may have approximations, it is quite safe to say that the dimetrodon was not concerned about the possibility of sail failure in case of high winds.

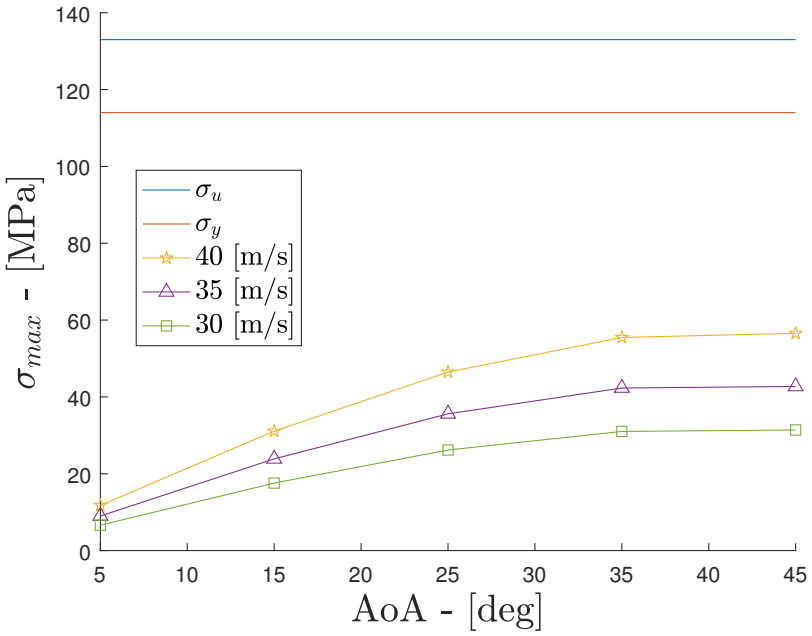

Figure 5.3: Maximum stress experienced by the sail's bones at various angles of attack and high wind speeds.

3 Evolution of the aerodynamic coefficients

A comparison between the lift and drag coefficients given by the rigid model and the flexible one is presented in Fig.5.4. For the sake of clarity, only the values corresponding to the deformed shape at 40 [m/s] are displayed, since the latter has the largest discrepancies with the rigid model. The relatively small fluctuations prove that that the sail is quite rigid. The decrease of the lift coefficient starting from 15 degrees is due to the progressive formation of a small inverse camber, that is visible when looking at the deformed shape of Fig.5.5. The phenomenon is less visible but still present for the drag coefficient, when looking at the curve beyond 35 degrees.

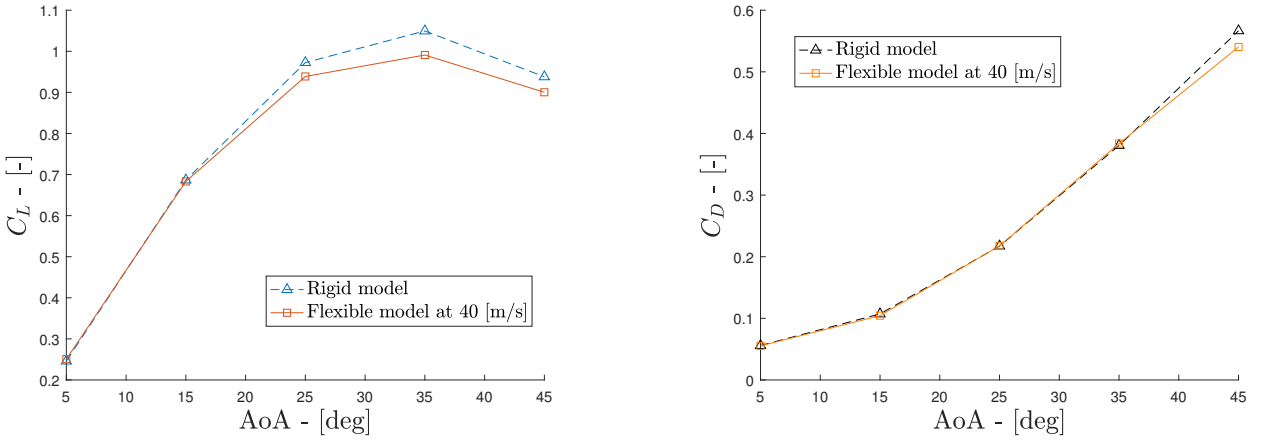

Figure 5.4: Variation of the lift and drag coefficients with the AoA, for the rigid model and the flexible one deformed at a wind speed of 40 [m/s].

An example of the deformation of the sail on the VLM model at a wind speed of 40 [m/s] and an angle of attack of 45 [deg] is represented on Fig.5.5. The scale is adapted for the sake of clarity, but it can be seen that even for those values of high wind speed and medium angle of attack, the maximum deformation is just above 5 [cm].

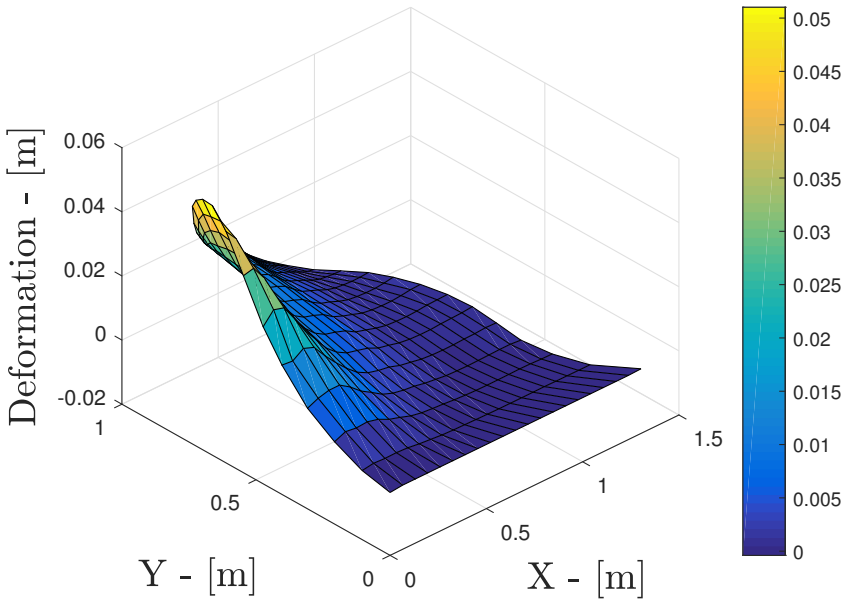

Figure 5.5: Sail deformation in the chordwise and spanwise direction in [m], for a wind speed of 40 [m/s] an angle of attack of 45 [deg].

Chapter 6

Stability analysis

The final step of this thesis is the coupling of the found aerodynamic loads to a static stability model so that the reaction of the dimetrodon in case of high wind can be predicted.

1 Static stability

Regarding the static stability model, two positions are considered:

The first one is the natural animal posture, inspired by the selected skeleton and by the existing reptiles. The body is assumed to be a cylinder, and since the model is scaled to a sail of 1 [m] high, its radius is approximated to 0.3 [m]. The legs are divided into two parts, and according to the gait of most reptiles, they form a right-angle at their connection. The part attached to the body is estimated to size 0.25 [m] as the vertical part is equal to the body radius. The mass of a full-grown specimen is estimated to be between 200 and 250 [kg] [11]. To be conservative, a weight of 200 [kg] is applied at the centre of gravity, which is located at the centre of the cylinder. The dorsal is finally placed at the top of the cylinder. Note that the body is not in contact with the floor, a very tiny gap separate the two.

The second position represents the animal's most likely reaction to the emergence of a strong disturbing moment. The legs are here fully stretched to maximize the stabilizing moment. Initially, the only forces are the dimetrodon's weight W and the vertical reaction forces V_A and V_B. The two configurations are represented in Fig.6.1.

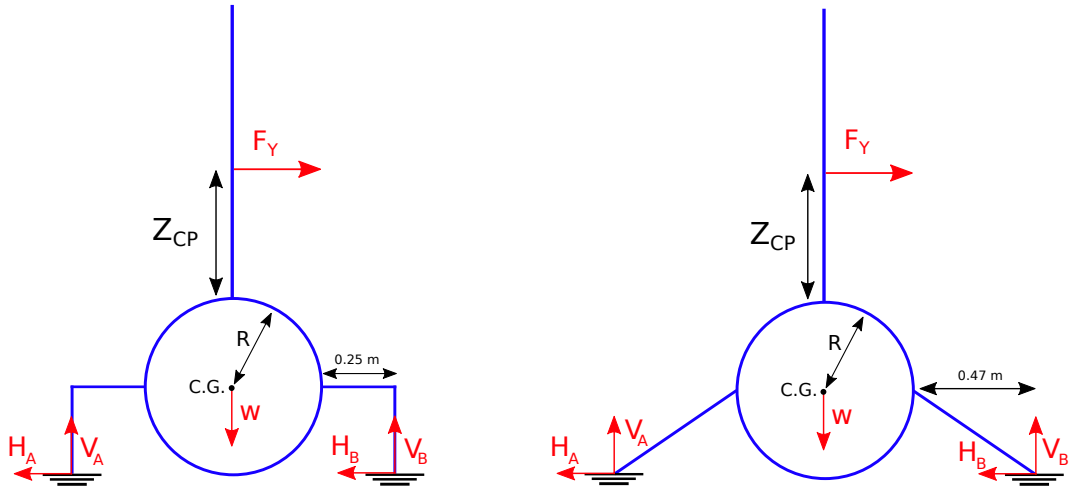

Figure 6.1: Schematic view of the stability model of the dimetrodon, in his natural position (left) and on his alerted position (right).

2 Aerodynamic loads consideration

The model is then subject to an overturning force F_Y, computed with the coefficient C_{F_Y} **found during the wind tunnel tests**. This force is applied at the centre of pressure, and its spanwise position Z_{CP} is determined by Eq.(3.9). Its variation with the angle of attack was represented in Fig.3.19.

The apparition of this new contribution induces two horizontal reactions forces at points A and B on Fig.6.1. The dimetrodon loses its stability and start tilting when the vertical reaction force at point A vanishes. The critical overturning force F_{Y_c} is obtained with the equilibrium of momentum at point B, equal to:

$$\sum M_B = (2R + Z_{CP}) \cdot F_{Y_c} - (0.25 + R) \cdot W = 0, \tag{6.1}$$

where R is the body radius and W the animal's weight. The critical overturning speed U_c defined as

$$U_c = \sqrt{\frac{2F_{Y_c}}{\rho C_{F_Y} S}} \tag{6.2}$$

with ρ the air density (here set to 1.225) and S the model's sail surface (equal to 0.92 [m^2]), can then be expressed as

$$U_c = \sqrt{\frac{2W(0.25 + R)}{(2R + Z_{CP})\rho C_{F_Y} S}}. \tag{6.3}$$

The dimetrodon's reaction by instinctively changing its legs position considered in the second case increases the stabilising moment and the previous equation becomes

$$U_c = \sqrt{\frac{2W(0.47 + R)}{(2R + Z_{CP})\rho C_{F_Y} S}}. \tag{6.4}$$

3 Results

The variation of the critical speed for the 2 configurations is described in Fig.6.2. As expected, U_c decreases as the angle of attack increases. At low angles of attack, the animal is safe from overturning since the critical speed is at an amplitude way higher than the maximum airspeed considered in this study, 40 [m/s], corresponding to critical weather conditions ("Hurricane force" on Beaufort scale). For the largest angles of attacks, the critical speed approaches and even passes below the limit meaning that the dimetrodon may tilt if it encounters a very strong side wind. However, if it reacts quickly and positions itself in its most stable posture, it can withstand winds up to 45 [m/s]. It then has a comfortable margin, since winds of this magnitude are hardly ever encountered.

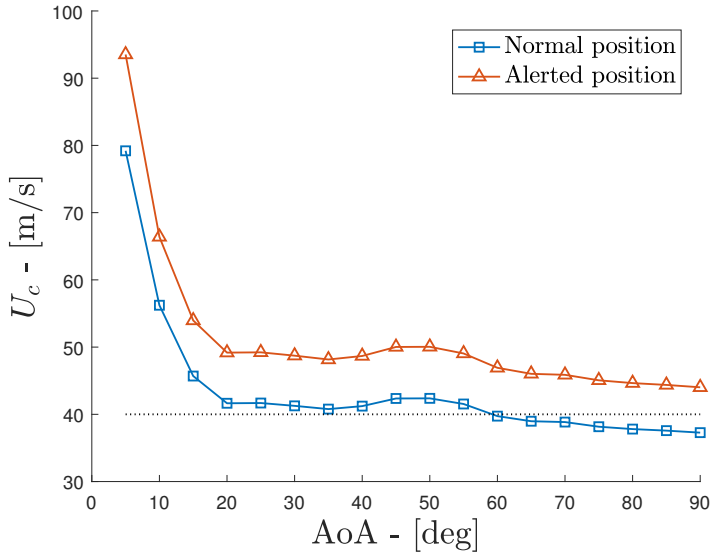

Figure 6.2: Variation of the critical wind speed with the angle of attack, for the normal and alerted positions.

As a conclusion, the dimetrodon's body position ensures him high stability and allows him to remain stable for most of the weather conditions he could encounter. Most of the time, the animal shouldn't need to adapt his position as the wind come up. In the case of stormy weather, it is highly probable that a change in the animal position would be enough to prevent overturning, due to its low centre of gravity and its heavy weight. Moreover, a change of angle of attack would definitely secure the animal. It means that the development of a sail for thermoregulation purposes did not compromise the pelycosaur's stability. Moreover, the bone structure ensures a strong resistance to failure, allowing the animal to live safely in all weather conditions.

Chapter 7

Conclusion

1 Present work

The objective of this thesis was to perform a numerical and experimental analysis of the flow around a neural spine sail to determine whether if it could endanger the pelycosaur's stability in case of high wind speeds. That fin located at the back of the animal appeared most probably to improve the thermoregulation of those large Paleozoic reptiles and had an impact on the aerodynamic profile since it represented a significant obstacle to the wind.

The first part of the work consisted in the implementation of the numerical model by using the vortex lattice method. This method relies mainly on Joukowski's equations for the computation of forces. The discretization is made by choosing the optimal number of panels in both chordwise and spanwise directions via a study of convergence on the aerodynamic coefficients. The domain length, as well as the wake model, were chosen adequately so that the wake influence was made sure to be well captured. The VLM is known to have limits in its accuracy, especially at high angles of attack since it uses the potential flow theory, ignoring the viscous effects due to its several strong assumptions. That is why the results obtained by this method needed to be validated.

In the second part of this thesis, an experimental model was realized and tested in the ULiège wind tunnel facility. A wood copy with the same geometry as the numerical model was built, and a high precision sensor was placed at its quarter chord. A support was also designed to avoid any disturbance in the measurements. The sensor being very sensitive, a corrector term has been computed to account for the unwanted internal stresses due to the moments applied on the *ATI Omega160*. Finally, a sufficiently high airspeed of 15 [m/s] was selected so that the aerodynamic coefficients do not vary anymore with the Reynolds number.
The results obtained in the wind tunnel vein could then be compared with the numerical ones. At low angles of attack (< 10 [deg]), the aerodynamic coefficients, as well as the estimation of the center of pressure position, are very close. Beyond those angles, the flow separation begins to occur, as confirmed by the flow visualisation experiment, and the results begin to slowly differ. It, however, stays relatively close as the angle of attack increases until it reaches 45/50 degrees. It then completely diverges and even gives unrealistic values, especially for the drag coefficient.

The third part of this thesis concerned the implementation of a flexible model using the finite element method. The latter aims to compute the displacements of the sail when subject to

aerodynamic loads, and estimate the corresponding internal stresses. The bones are modelled as 3D beams and then divided into elements. Since the dimetrodon's bone properties could not be found in the literature, the density, Young's modulus and Poisson's ration of a common human bone were used. The geometry used in the previous step has here been divided into 37 bones, according to the selected skeleton and the aerodynamic loads computed by the VLM are then applied following the lift distribution. The loads are considered to be directly transferred from the skin to the bones. The optimal number of division on each beam is found by performing a convergence study and by making a compromise between accuracy and computational cost.

A coupling of the FEM and VLM models could then be implemented so that the aerodynamic loads of a numerical flexible model could be computed at various airspeeds and angles of attack. The sail deforms due to the initial aerodynamic loads, involving a modification in its aerodynamic characteristics. The sail eventually reaches a stable deformed shape, which actually features a maximum displacement of fewer than 6 centimetres, showing a quite rigid behaviour. The internal stresses could then be estimated, and the bone experiencing the most important stresses was always the first one, representing the leading edge of the sail. It however always stayed far from the yield strength, even at high angles of attack and at stormy weather conditions.

Finally, a stability analysis was performed on a complete model of the dimetrodon estimating its dimensions using the selected skeleton and using the estimated weight of a full-grown specimen. Based on that information, two static models were built, one considering the natural position of the animal, based on the skeleton and the existing reptiles, and one representing the most stable position that it could take by reacting to a destabilizing force.
The latter expressed throughout this report as F_Y, is then computed for various airspeeds and angles of attack using the coefficient found by the wind tunnel and applied at the position of the corresponding centre of pressure. Using the equilibrium equation, the critical wind speed that creates a force high enough to cause the dimetrodon to topple could then be calculated. Its value at low angles of attack was very high and thus suggest that the reptile was stable even at critical weather conditions. It then decreases fastly as the angle of attack with respect to the free stream increases. The lowest critical wind speed, found when the dimetrodon is at the maximum angle of attack, is just below 40 [m/s], corresponding to the worst weather conditions on Beaufort scale ("Hurricane force"), and is considered as exceptional.
It can then be concluded that the heavy weight and the low centre of gravity position of the dimetrodon due to its body configuration allowed the reptile to safely move in most of the weather conditions. The aerodynamic loads were distributed on the elongated bones in a way that the yield strength was never approached. As a final word, this thesis tends to confirm that nature is well designed.

2 Future work

2.1 Modeling improvements

The different models may be improved to increase the reliability of the results. It has been pointed out that the potential flow theory works under several strong assumptions, such as the inviscid nature of the flow. If the wind tunnel model allowed to understand the limits of the vortex lattice model, a second validation using a complete CFD analysis of the flow around the sail could be useful, especially concerning the lift distribution that could not be confirmed by

the experimental tests.
The replica of the sail used in the wind tunnel was idealized as a flat plate with a certain thickness, which should not agree with the probably more complex original shape.
In addition, it could be interesting to study the body contribution in the aerodynamic loads. The latter has been neglected in this thesis' models.
For the finite element analysis, the deformations and stresses were computed using the classic beam theory, which is simple in implementation but less accurate than a complete finite element modelling of all the bones. This could be done to confirm that the reptile was safe from sail damages in case of stormy weather.

2.2 Biological features

The lack of information concerning the pelycosaurs biological features in the literature forced some assumptions, especially concerning the bone properties. The genuine Young's modulus, Poisson's ratio and density would improve the accuracy of the finite element model. However, the relatively large margin concerning the stresses and the low deformation suggest that it would not completely disagree with this thesis's conclusions.
Moreover, except for the bones configuration, the literature doesn't give many details about the sail composition, including the skin characteristics. The latter could have significant impacts on the sail's aerodynamic profile and rigidity, depending on its thickness and properties. The elongated bones were supposed to be clamped to the spine, but it is possible that the dimetrodon could interact with its sail by the means of muscles, allowing him to modify its behaviour when exposed to high wind speeds.

Bibliography

[1] *Dimetrodon*. http://www.prehistoric-wildlife.com/species/d/dimetrodon.html. Accessed: 2019-02-11.

[2] J. Katz and A. Plotkin. *Low-speed Aerodynamics*. 2nd ed. McGraw-Hill Book Co, 1991.

[3] T. Lambert and G. Dimitriadis. *Induced Drag Calculations with the Unsteady Vortex Lattice Method for Cambered Wings*. 2016.

[4] Université de Liège. "The University of Liège Wind Tunnel Facility- Technical description". 2009.

[5] *F/T Sensor: Omega160*. https://www.ati-ia.com/products/ft/ft_models.aspx?id=Omega160. Accessed: 2019-02-28.

[6] Dae Kun Kwon and Chang-Koon Choi. *Wind tunnel blockage effects on aerodynamic behavior of bluff body*. 1998.

[7] V. Terrapon and T. Andrianne. "Lecture Slides: Aerodynamics-Introduction". page 54. 2018.

[8] Charlotte A. Brassey and William I. Sellers. *Finite element modelling versus classic beam theory: comparing methods for stress estimation in a morphologically diverse sample of vertebrate long bones*. 2013.

[9] M. Kutz. *Standard Handbook of Biomedical Engineering and Design*. 1st ed. McGraw-Hill Book Co, 2003.

[10] *The Beaufort Scale*. https://www.rmets.org/resource/beaufort-scale. Accessed: 2019-04-10.

[11] *Dimetrodon*. http://paleodico.wifeo.com/dimetrodon.php. Accessed: 2019-03-25.